

The Influence of Pine Island Ice Shelf Calving on Melting

A. T. Bradley¹, D. T. Bett¹, P. Dutrieux¹, J. De Rydt², P. R. Holland¹

¹British Antarctic Survey, High Cross, Madingley Road, Cambridge CB3 0ET, UK

²Department of Geography and Environmental Sciences, Northumbria University, Newcastle upon Tyne, UK.

Key Points:

- Melting of Pine Island Ice Shelf is sensitive to calving because of a seabed ridge beneath it.
- The melt response to calving has a strong sensitivity on the cavity geometry.
- Calving may be an important contribution to the ice-ocean sensitivity of the Antarctic Ice Sheet.

13 **Abstract**

14 A seabed ridge beneath Pine Island Ice Shelf (PIIS), in combination with the ice draft
 15 above it, form a topographic barrier, restricting access of warm Circumpolar Deep Water
 16 to a cavity inshore of the ridge, and thus exerting an important control on basal ab-
 17 lation of the PIIS. In addition, PIIS has recently experienced several large calving events,
 18 and further calving could significantly alter the cavity geometry. Changes in the ice front
 19 location might lead to a relaxation of the topographic barrier, and thus significantly change
 20 basal melt rates. Here, we consider the impact of past, and possible future, calving on
 21 PIIS melt rates. We use a high-resolution ocean model to simulate melting in both an
 22 idealized domain whose geometry captures the salient characteristic features of PIG, and
 23 a realistic geometry which accurately resembles it, to explore this question. The ideal-
 24 ized simulations reveal that the melt response to calving has a sensitive dependence on
 25 the thickness of the ridge-draft gap and inform our interpretation of the realistic sim-
 26 ulations, which demonstrate that modelled melt rates under PIIS do not respond sig-
 27 nificantly to recent calving events. However, the mean melt rate increases approximately
 28 linearly with further calving, and are amplified by approximately 10% relative to present
 29 day the ice front reaches the ridge crest, which will take less than one decade if ice front
 30 retreat maintains its present rate. This provides strong evidence that calving may rep-
 31 resent an important, but as yet unexplored, contribution to the ice-ocean sensitivity of
 32 the West Antarctic Ice Sheet.

33 **Plain Language Summary**

34 Pine Island Glacier has a large seabed ridge beneath its floating extension, referred
 35 to as Pine Island Ice Shelf. The combination of the ridge and ice shelf above it reduce
 36 the amount of relatively warm water that is able to reach the ice shelf, therefore restrict-
 37 ing its melting. However, the ice shelf has also lost large sections from its front in recent
 38 years, in a process referred to as calving. In this paper, we investigate the effect of these
 39 two processes: how does calving affect the melt rates on Pine Island Ice Shelf. Using nu-
 40 matical simulations of the ocean flow beneath the ice shelf, we identify a potentially high
 41 sensitivity of melt rates on calving, depending on the cavity geometry. In addition, our
 42 simulations suggest that the melt rate has an approximately linear dependence on the
 43 distance that the ice front retreats after any further calving events. These results pro-
 44 vide strong evidence that changes in the melting of ice shelves in response to calving might
 45 represent an important contribution to the response of West Antarctica in a changing
 46 climate.

47 **1 Introduction**

48 Pine Island Glacier (PIG), located in the Amundsen Sea sector of Antarctica, is
 49 one of the fastest changing glaciers worldwide. A sustained increase in ice discharge and
 50 surface velocity, as well as significant grounding line retreat, have been documented since
 51 satellite measurements began in the 1990s (Rignot et al., 2002; Rignot, 2008; Rignot et
 52 al., 2011; Mouginot et al., 2014; Gardner et al., 2018). PIG has experienced a 70% in-
 53 crease in grounding line ice flux and a close to doubling of surface velocity between 1974
 54 and 2013 (Mouginot et al., 2014), while its grounding line retreated some 31 km at its
 55 centre between 1992 and 2011 (Rignot et al., 2014). Increased basal melting of Pine Is-
 56 land Ice Shelf (PIIS) – the floating extension of the PIG’s grounded ice – has been im-
 57 plicated as a key driver of these changes (Shepherd et al., 2004; Pritchard et al., 2012;
 58 Rignot et al., 2019): ice shelves offer a resistive stress (commonly referred to as ‘buttr-
 59 essing’) that restrains the flow of grounded ice; increased basal melting can reduce ice shelf
 60 volume and thus the buttressing they are able to provide (Gudmundsson, 2013; Reese,
 61 Gudmundsson, et al., 2018; Gudmundsson et al., 2019; Gagliardini et al., 2010; Gold-
 62 berg et al., 2019; De Rydt et al., 2021).

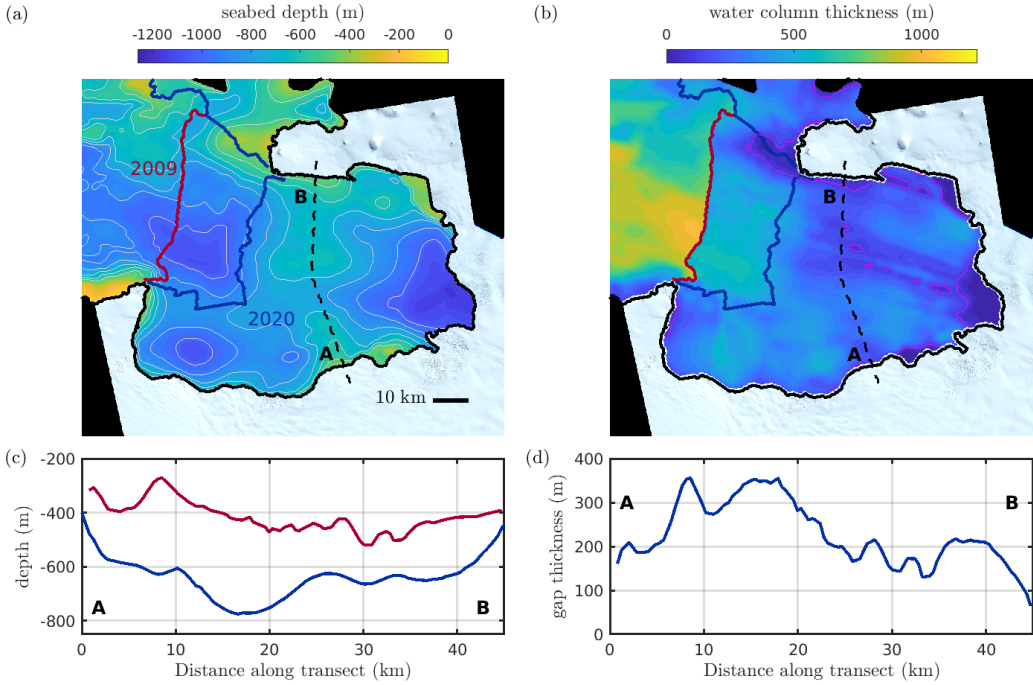


Figure 1. (a) Seabed depth and (b) water column thickness under Pine Island Ice Shelf and in Pine Island Bay (colors) from Dutrieux et al. (2014). Also shown are the locations of the ice front in 2009 (red line) and 2020 (blue line), as indicated in (a). The solid black line indicates the grounding line from Joughin et al. (2010), and the background image is a Sentinel 2 mosaic from November 2020. The black dashed line indicates the approximate location of the crest of the seabed ridge. The magenta contour in (b) corresponds to 125 m water column thickness. (c) Seabed bathymetry (blue) and ice draft (red) taken along the black dashed line in (a)–(b). (d) Plot of the ridge-draft gap measured along the black dashed black line in (a) [i.e. the difference between the red and blue lines in (c)].

In the Amundsen Sea sector, Circumpolar Deep Water (CDW) provides the main source of heat that drives ice shelf melting. The pycnocline that separates CDW from Winter Water above it remains mostly above the level of the continental shelf break in the Amundsen Sea (Jacobs et al., 2015; Heywood et al., 2016). CDW is therefore able to spill onto the continental shelf and reach ice shelf cavities, providing significant heat to the adjacent ice shelves for melting. The flux of CDW that is able to spill over the continental shelf is a good proxy for the depth of this pycnocline; this flux (and thus the depth of the pycnocline) is not constant, but varies significantly on decadal timescales (Jenkins et al., 2018). Years with a deeper pycnocline, and thus thinner CDW layer, tend to result in lower meltwater fluxes from ice shelves, and vice versa (Jacobs et al., 2011; Dutrieux et al., 2014).

However, for PIG specifically, this simple ‘pycnocline depth’ picture is complicated by the presence of a seabed ridge in the ice shelf cavity. This ridge is located several tens of kilometers downstream of the grounding line, and protrudes up to three hundred meters above the neighboring seabed (figure 1a). In combination with the ice shelf directly above it, the ridge acts as a topographic barrier, restricting the access of CDW to an inner cavity which has formed between the ridge and the ice shelf since the grounding line retreated from this ridge in a process initiated in the late 1940s (Jenkins et al., 2010; De Rydt

et al., 2014; De Rydt & Gudmundsson, 2016; Smith et al., 2017). This cavity geometry means that, at present, the strength of the topographic barrier (i.e. how much its presence affects ice shelf melting) is strongly dependent on the pycnocline depth: at its shallowest, the pycnocline sits above the depth of the ridge crest, and a large amount of modified CDW is able to spill into the inner cavity (Dutrieux et al., 2014); in contrast, at its lowest, the pycnocline sits some way below the ridge crest and CDW access is severely restricted. The presence of the seabed ridge thus contributes to the strong sensitivity of PIIS melting to hydrographic conditions in Pine Island Bay (PIB): Dutrieux et al. (2014) reported that the total freshwater flux from the fast flowing part of PIG in 2009 (80 km^3), when the pycnocline was at its shallowest depth on record (Webber et al., 2017), was more than double its value in 2012 (37 km^3), when the pycnocline was at the second-lowest recorded depth.

In addition to its unique topographic control on melt rates, the recent calving of PIIS also stands out amongst Amundsen Sea terminating ice shelves. Mass loss from the Antarctic ice sheet is dominated by calving and melting (Rignot et al., 2013); in equilibrium, these losses must balance the upstream accumulation of ice. The recent retreat of the ice front of PIIS, however, suggests that the calving rate is far higher than would be required to maintain an equilibrium. The ice front retreated approximately 26 km between 2009 and 2020 (figure 1a), with the majority of this retreat happening over the period 2015–2020 (Lhermitte et al., 2020; Joughin et al., 2021). This corresponds to a more-than-doubling of the calving rate, from approximately 4 km year^{-1} prior to 2015, to approximately 9 km year^{-1} in the period 2015–2020 [the flow speed at the ice front, for context, is approximately 5 km year^{-1} (Joughin et al., 2021)].

As of 2020, the ice front is located approximately 20 km downstream of the ridge (figure 1a), meaning that the ice front is now closer to the ridge crest than it is to the location of the ice front in 2009. The loss of buttressing associated with this retreat of the ice front can explain the acceleration of PIG since 2015 (Joughin et al., 2021). However, given that the topographic barrier to CDW relies on the combination of ice draft and seabed ridge, the recent calving events beg the following question: has recent calving of PIIS relaxed the topographic barrier, leading to significant changes in melting? Increased melting of its ice shelf might lead to further reductions in ice shelf volume and thus reduced buttressing, ultimately leading to ice shelf acceleration, thinning, and grounding line retreat.

In addition to considering the effect on melt rates of calving events that have already happened, one might also consider how melt rates might respond to possible future calving events. It has been suggested that further significant calving of PIIS is likely, since damage to the ice shelf that has already occurred is thought to have preconditioned PIIS to collapse (Lhermitte et al., 2020). Furthermore, if calving does indeed affect melting, one could imagine a ‘calving-melting’ feedback loop in which calving enhances ice shelf melting, leading to reduced buttressing and thus ice acceleration, ultimately resulting in ice shelf damage and further calving. Here, we test the first link in this chain of events.

In this study, we assess how, and why, melt rates on PIIS might respond to past, and possible future, calving events. To do so, we use a numerical general circulation model to simulate the ocean circulation in both an idealized setup whose geometry captures the salient characteristic features of PIIS and its cavity (most notably, a seabed ridge whose crest is in proximity to the ice shelf base), and a realistic setup whose geometry closely matches real world conditions for PIIS. We begin in §2 with a description of the idealized experiments, setting out details of the ocean model used and the experimental setup. We identify one such experiment as a baseline, and present the results of this experiment in §3. In §4, we describe how, and why, the melt rate varies as calving proceeds from this baseline. In the following two sections, we discuss how the picture of melt response to calving presented in §4 changes when the cavity geometry (§5) and far field

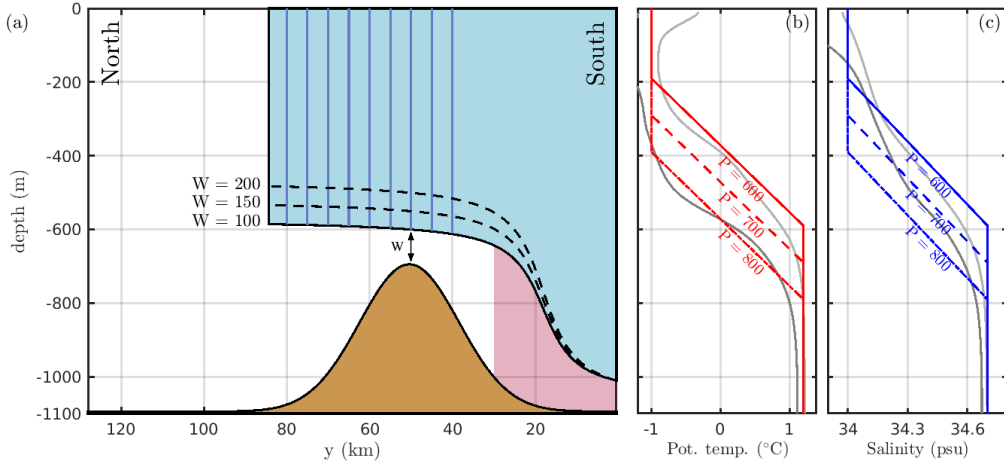


Figure 2. (a) Schematic diagram of the experimental setup. The domain is uniform in the zonal direction (into the page), with extent 48 km. The ocean domain consists of the gridded area, which is bordered by a static ice shelf in $y < 84$ km (shaded blue) and a seabed (shaded brown), which features a prominent ridge. Solid, dashed and dot-dashed black curves indicate the location of the ice shelf base for $W = 100$ m, $W = 150$ m, and $W = 200$ m, respectively, as labelled [the profile of the ice shelf base is defined in equation (4)]. Solid blue lines indicate the series of ice front positions considered, which are located at $80, 75, 70, 65, 60, 55, 50, 45,$ and 40 km offshore of the southern end of the domain at $y = 0$ km (the y -axis is oriented in this way for consistency with the orientation of PIG in practice, see figure 1). The shaded red region indicates the inner cavity, defined as the area within 30 km of the southern end of the domain. (b) Temperature and (c) salinity profiles used in the experiments. Different line styles correspond to different values of the pycnocline depth parameter P as follows: $P = 600$ m (solid), $P = 700$ m (dashed), $P = 800$ m (dot-dashed). Light and dark gray lines correspond to temperature and salinity profiles taken from conductivity, temperature, and depth measurements in Pine Island Bay during the austral summers of 2009 (Jacobs et al., 2011) and 2012 (Dutrieux et al., 2014), respectively.

ocean conditions (§6) are altered. In §7 we describe and present the results of the realistic experiments. Guided by the results of the idealized experiments, we assess the expected response of melt rates under PIIS to recent, and possible future, calving events. Finally, we discuss the implications of our results in §8, and summarize the key results in §9.

2 Idealized Experiment Details

In this section, we describe the experiments performed in an idealized setup, which we refer to as ‘idealized experiments’. The idealized experiments have essentially the same setup as De Rydt et al. (2014), albeit it with an updated model configuration, and sections of the ice shelf removed to simulate calving. The domain features a seabed ridge and ice shelf (see figure 2a), which are both uniform in the zonal direction (and thus so too is the ridge-draft gap between them). In practice, however, the ridge-draft gap is non-uniform (figure 1c–d); to capture the effect of this variation, we consider the melt response to calving for different thicknesses of the ridge-draft gap. We also consider several different far-field ocean conditions (‘hydrographic forcings’): as discussed in §1, PIIS melt

149 rates have a sensitive dependence on the hydrographic forcing, via the depth of the py-
 150 cnocline; we therefore postulate that the melt response to calving might similarly have
 151 a sensitive dependence on the hydrographic forcing, and investigate this effect. The role
 152 of these idealized experiments, with a highly simplified geometry, is to allow us to iso-
 153 late the important roles that the thickness of the ridge-draft gap and the hydrographic
 154 forcing play in the melt response to calving, as well as elucidate the physical mechanisms
 155 responsible for these changes.

156 We perform a total of 90 idealized experiments, each corresponding to a unique triplet
 157 of parameters which describe the thickness of the ridge-draft gap, the hydrographic forc-
 158 ing, and the position of the ice front. These parameters are described in the following
 159 two sections. By systematically shifting the ice front towards the (fixed) grounding line
 160 between experiments, we simulate calving (and use that name to describe this procedure),
 161 but stress that our model includes neither calving dynamics, nor associated processes
 162 such as mélange formation. Within each experiment, we solve for the three-dimensional
 163 ocean circulation and associated melt rates simultaneously using the Massachusetts In-
 164 stitute of Technology general circulation model (MITgcm) (Marshall et al., 1997). Other
 165 than removing sections of the ice shelf, the ice shelf geometry does not change between
 166 experiments. Ice shelves themselves enter the ocean model via the exchange of heat and
 167 salt at the ice-ocean interface and a steady pressure loading on the ocean surface, i.e.
 168 ice dynamics are not taken into consideration when determining the cavity geometry. A
 169 steady description of ice shelves is sufficient to assess the response of melt rates to ice
 170 shelf calving, which occurs on a timescale much shorter than that on which the ice re-
 171 sponds dynamically to perturbations in melting. In the following sections, we provide
 172 further details of the ocean model and experimental setup, including the motivation for
 173 our choices of parameters.

174 2.1 Details of Ocean Model

175 The MITgcm is a z-level general circulation model which includes a partial-cell treat-
 176 ment of topography, allowing an accurate description of both the seabed and ice draft.
 177 Our model grid consists of 110 layers with a vertical spacing of $dz = 10$ m, and a hor-
 178 izontal resolution of $dx = 400$ m. We use the MITgcm in hydrostatic mode with an im-
 179 plicit nonlinear free surface scheme, a third-order direct space-time flux limited advec-
 180 tion scheme, and a non-linear equation of state (McDougall et al., 2003). The Pacanowski-
 181 Philander (Pacanowski & Philander, 1981) scheme parametrizes vertical mixing. Con-
 182 stant values of 15 and $2.5 \text{ m}^2 \text{ s}^{-1}$ are used for the horizontal Laplacian viscosity and hor-
 183 izontal diffusivity, respectively. The equations are solved on an f -plane with $f = -1.4 \times$
 184 10^{-4} s^{-1} .

185 In each experiment, the simulation is run for twelve months, using a timestep of
 186 30 seconds. After this spin-up time, the configuration is quasi-steady state. In partic-
 187 ular, the field of melt rate is everywhere within 95% of its final value after three months
 188 in each experiment considered here. All results presented here are averaged over the fi-
 189 nal two months of the simulations.

190 As mentioned, ice shelves impact on the ocean state via the exchange of heat and
 191 salt at the ice-ocean interface. This exchange is described using the so-called ‘three-equation
 192 formulation’ (Holland & Jenkins, 1999), whose implementation in MITgcm has been de-
 193 scribed thoroughly elsewhere (Losch, 2008; De Rydt et al., 2014; Dansereau et al., 2014,
 194 for example) and so we do not describe it in detail here. It is useful to note, however,
 195 that thermal exchange across the ice-ocean interface is typically dominated by latent heat
 196 [over heat conduction into the ice (Holland & Jenkins, 1999)]; in the case of negligible
 197 heat conduction, the three-equation formulation for melting reduces to

$$198 \dot{m} = \frac{c_p \gamma_T (T - T_b)}{L}, \quad (1)$$

where, \dot{m} is the melt rate. In (1), T is the temperature in the mixed layer adjacent to the ice base, which is considered to have a thickness dz everywhere, and T_b is the temperature at the ice shelf base, which must be at the local (depth and salinity dependent) freezing point. We refer to the difference of these temperatures, $T - T_b$, as the thermal driving. The quantity γ_t is a heat exchange-coefficient, which parametrizes exchange between the mixed layer and the ice shelf base. In our version of the MITgcm, we assume that γ_t has a linear dependence of u^* , the ocean speed in the viscous boundary layer that forms adjacent to the ice shelf base. We can therefore write

$$\dot{m} \propto u^*(T - T_b). \quad (2)$$

We shall return to equation (2) when diagnosing the mechanisms responsible for the melt rate response to ice shelf calving.

We use parameter values from Holland and Jenkins (1999) in (1)–(2), except for the drag coefficient in the three-equation formulation of melting, which is set to 4.5×10^{-3} . As discussed in §7, this value is more appropriate for Pine Island Glacier than the value of 2.5×10^{-3} suggested by Holland and Jenkins (1999).

2.2 Ice Shelf Geometry and Seabed Bathymetry

The geometry of the idealized setup is shown schematically in figure 2a. It is uniform in the zonal direction, along which the x -axis is aligned, and the y -axis is aligned along the meridional direction. Note that although PIG is aligned approximately east-west, we orient this idealized model north-south, as is standard (Grosfeld et al., 1997; De Rydt et al., 2014) and results are independent of this choice of orientation.

The seabed has a shifted Gaussian profile,

$$b(x, y) = -1100 + 400 \exp \left[-\frac{(y - 50 \times 10^3)^2}{2\sigma^2} \right], \quad (3)$$

where $\sigma = 12$ km is the length scale over which this profile decays towards zero. The profile (3) corresponds to a ridge that peaks at a height of 400 m above the surrounding bathymetry. This peak occurs 50 km from the southern end of the domain at $y = 0$ km, which we consider to be the grounding line (figure 2a).

In reality, the variability in both PIIS draft and the height of the seabed ridge result in a ridge-draft gap that varies between approximately 100 m at its thinnest, to greater than 300 m at its thickest (figure 1c–d). Since we use the same, zonally uniform, seabed geometry (and, in particular, the same ridge height) in all of our idealized experiments, we aim to gain insight into the effect of variation in the ridge-draft gap by considering several different values of W – the vertical distance between the crest of the seabed ridge and the ice shelf base (figure 2a). In our setup, W enters the model only via the ice profile; following De Rydt et al. (2014), we use an ice shelf draft given by

$$H(y) = \begin{cases} \left(\frac{310+W}{2.64} \right) \tan^{-1} \left(\frac{y}{5882} \right) - 3 & \text{for } y < y_f, \\ 0 & \text{for } y \geq y_f. \end{cases} \quad (4)$$

Here y_f is the variable location of the ice front (see below). We stress that the ice draft profile (4) is not obtained from ice dynamics considerations, but selected for its qualitative similarity to PIIS: it includes a flatter section offshore of the ridge and a steeper section inshore of the ridge, thus resembling variations in the basal slope that have been inferred from radar and satellite data. Note that the combination of the bathymetry (3) and ice shelf draft (4) means that the water column thickness is small, but nonzero at the grounding line (figure 2a); this is because the MITgcm requires at least two grid cells in the vertical direction to permit horizontal transfer.

We consider three different values of W here: $W = 100$ m, $W = 150$ m, and $W = 200$ m. The smallest value, $W = 100$ m, corresponds to the minimum observed ridge-draft gap under PIIS (figure 1d), while the largest value, $W = 200$ m, corresponds to an upper bound, above which there is little melt response to calving, as we shall see.

As mentioned, the front position y_f is systematically reduced between experiments to simulate calving. We consider a total of ten different ice front positions, using $y_f = 84, 80, 75, 70, 65, 60, 55, 50, 45$, and 40 km, which correspond to calved lengths of $l_c = 0, 4, 9, 14, 19, 24, 29, 34, 39$, and 44 km, respectively. Those experiments with $l_c = 0$ km are referred to as ‘uncalved’ experiments, serving as a benchmark against which results for $l_c > 0$ km are compared. There are both pragmatic and physical reasons for choosing this particular range of values for l_c : the setup with $l_c = 0$ km has an ice shelf whose length is approximately equal to the observed distance of the ice front from the PIG grounding line in 2009, before significant calving took place in the late 2010s; the largest value, $l_c = 44$ km, is chosen as a compromise between allowing us to consider scenarios in which the ice front has been retreated significantly beyond the ridge, whilst retaining a large area that is shared by each experiment (as we discuss further in §3, the area over which melt rates are averaged must be invariant to calving for a robust assessment of the melt response to calving).

2.3 Hydrographic Forcing

For each unique value of W and l_c , we perform three experiments, each with a different hydrographic forcing. The range of these hydrographic forcings covers that which is observed in practice (see below). Comparing the results of these experiments gives us an indication of the sensitivity of our results to hydrographic forcing.

The hydrographic forcing is imposed on the model by means of a restoring boundary condition at the northern end of the domain ($y = 128$ km in figure 2a): at this boundary, the temperature and salinity are restored to specified vertical profiles, shown in figure 2b and c, respectively, over a distance of five horizontal grid cells (total length 2 km) with a restoring timescale that varies from 12 hours at the boundary to 60 hours in the interior. The specified temperature and salinity profiles are piecewise linear functions of depth: they are constant in both an upper (temperature -1°C , salinity 34 PSU) and lower layer (temperature 1.2°C , salinity 34.7 PSU), and these layers are separated by a pycnocline of 400 m thickness, across which the temperature and salinity vary linearly. The pycnocline begins at a variable depth P (a higher P corresponds to a deeper pycnocline), which parametrizes the entirety of the temperature and salinity profiles (figure 2b, c); the three hydrographic forcings we consider have $P = 600$ m, 700 m, and 800 m.

These piecewise linear profiles are approximations to typical conditions for PIB (Jacobs et al., 1996; Dutrieux et al., 2014; Jenkins et al., 2018) (figure 2b–c). As mentioned, the record of hydrographic conditions in PIB has revealed significant variability in the depth of the pycnocline on interannual timescales (Dutrieux et al., 2014); the profiles with $P = 600$ m and $P = 800$ m are approximations to profiles observed in PIB in the years 2009 and 2012, respectively (figure 2b, c). These two years approximately span the range of observed conditions: in 2009, the average depth of the pycnocline was at its shallowest level on record, while in 2012 the average depth of the pycnocline was at its second-deepest level on record (Webber et al., 2017).

In summary, we perform a total of 90 idealized experiments. Each is uniquely identified by a (W, P, l_c) triplet, where $W \in \{100, 150, 200\}$ m, $P \in \{600, 700, 800\}$ m, and $l_c \in \{0, 4, 9, 14, 19, 24, 29, 34, 39, 44\}$ km. We consider the experiment with $W = 100$ m, $P = 600$ m, and $l_c = 0$ km to be the baseline; this corresponds to the extreme scenario with the narrowest ridge-draft gap (the strongest topographic barrier), the hydrographic forcing with the shallowest pycnocline (thickest CDW layer), and an

uncalved ice shelf. In the following section, we describe the results of the baseline experiment. In §4, we describe the results of applying the calving perturbation to the baseline, presenting results of those experiments with $W = 100$ m, $P = 600$ m, $l_c > 0$ km; i.e. we describe the melt response to calving for $W = 100$ m, $P = 600$ m. In §5 and 6, we respectively describe how the melt response to calving changes for the different values of W and P considered here.

300 3 Results for the Baseline Experiment ($W = 100$ m, $P = 600$ m, 301 $\ell_c = 0$ km)

302 In this section, we describe the results for the baseline experiment with $W = 100$ m,
303 $P = 600$ m, which correspond to the solid lines in figure 2, and $l_c = 0$ km. Before we
304 proceed, we introduce the ‘inner cavity’ – the area of the ocean domain that is located
305 within 30 km of the southern boundary (indicated by the red-shaded region in figure 2a).
306 We use the mean melt rate in the inner cavity, referred to henceforth as the ‘inner cav-
307 ity melt rate’, as a single metric to quantify changes in melt rate with calving. Since the
308 melt rate is highly spatially variable (see below) it is necessary to consider a fixed area
309 that is common to each experiment when assessing changes in melt rate with calving.
310 Indeed, averaging over the whole shelf, for example, would make smaller shelves appear
311 to have anomalously large melt rates, since the region of high melt close to the ground-
312 ing line would occupy a greater proportion of the entire shelf. Our choice of 30 km in
313 this definition reflects a compromise between enabling simulations in which the ice front
314 is retreated a significant distance beyond the ridge to be included (the smallest shelf we
315 consider must be larger than the inner cavity, if the entirety of the inner cavity is to be
316 included in each experiment), and considering a reasonably large section of the uncalved
317 ice shelf over which the melt rate is averaged. Crucially, this choice includes the region
318 adjacent to the grounding line, where changes in melt rate are particularly important
319 for the dynamics of the grounded ice sheet (Seroussi et al., 2014; Arthern & Williams,
320 2017). Although the absolute values of the inner cavity melt rate *are* dependent on the
321 length of region chosen in its definition, we verified that the trends and key results pre-
322 sented here are independent of this choice.

323 Ice-ocean properties that characterize the baseline simulation are shown in figure 3.
324 Melt rates (figure 3a) are below 20 m year⁻¹ everywhere, except for a region located within
325 20 km of the grounding line, where the melt rate reaches a maximum of 120 m year⁻¹.
326 The average melt rate over the whole shelf is approximately 20 m year⁻¹. While this is
327 lower than the value of 33 ± 2 m year⁻¹ that was estimated by Jenkins et al. (2010) based
328 on observations in PIB in 2009, to which the $P = 600$ m case corresponds, this discrep-
329 arity is in the expected direction: the baseline simulation corresponds to the extreme sce-
330 nario in which the ridge-draft gap is set everywhere to the minimum gap that is observed
331 in practice, impeding the supply of warm water across the ridge. The melt rate is pro-
332 portional to the product of the ice-ocean mixed layer circulation and thermal driving [see
333 equation (2)]; while the circulation is vigorous everywhere inshore of the ridge, high melt
334 rates are restricted to the area south of $y = 20$ km: to the north of $y = 20$ km, a cold
335 and fresh meltwater plume sits adjacent to the ice-ocean interface (figure 3e) and the tem-
336 perature difference between the ocean and ice base is therefore much smaller than to the
337 south of $y = 20$ km, where the ice is adjacent to warm water.

338 When the ice shelf is calved in the subsequent simulations, the only a priori im-
339 posed change on the experiment is the water column thickness in those regions of the
340 domain in which the ice shelf is removed (the resulting buoyancy forcing also changes,
341 but this emerges from the simulation *a posteriori*). It is therefore instructive to consider
342 the effect of changes in water column thickness, which influence the flow only through
343 barotropic dynamics; we shall therefore use a primarily barotropic framework to diag-
344 nose the melt response to calving.

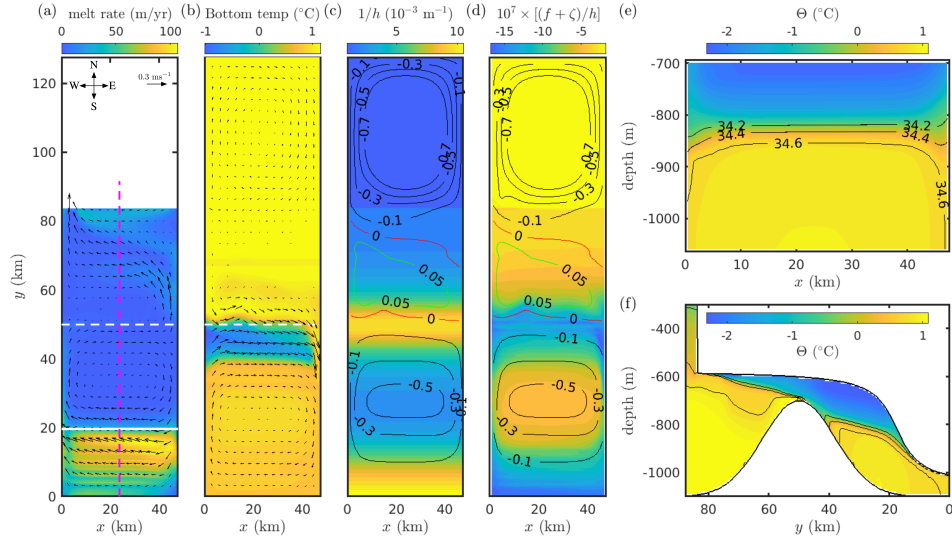


Figure 3. Ice-ocean properties that characterize the baseline experiment, with $W = 100 \text{ m}$, $P = 600 \text{ m}$, and $\ell_c = 0 \text{ km}$. (a) Melt rate (colors) and ocean velocities (arrows, every fifth velocity vector is plotted), averaged over the three grid cells adjacent to the ice-ocean interface. White areas correspond to open ocean. The white dashed line indicates the location of the ridge crest; the white solid line indicates $y = 20 \text{ km}$, along which the section in (e) is taken; and the magenta dashed line indicates the center line $x = 24 \text{ km}$, along which the section in (f) is taken. (b) Ocean temperature (colors) and velocity (arrows) averaged over the three grid cells closest to the seabed. The scale bar for velocity vectors in (a) is also appropriate for (b). (c) Inverse water column thickness $1/h$ and (d) barotropic potential vorticity (colors) alongside barotropic stream function (contours, in units of Sv) at levels 0.05 (green) 0 (red), -0.1, -0.3, -0.5, and -0.7 Sv (all black). (e) Zonal cross-section taken at $y = 20 \text{ km}$ up to the ice shelf base, showing potential temperature (Θ) in $^\circ\text{C}$ and salinity contours at the 34.2, 34.4, and 34.6 PSU levels, as indicated. (f) Meridional cross-section of temperature and salinity [with colors and contours as in (d)], taken along the centerline $x = 24 \text{ km}$.

345 Barotropic velocities $\hat{\mathbf{u}} = (\hat{u}, \hat{v})$ must satisfy the barotropic potential vorticity (BPV)
 346 equation [see Patmore et al. (2019), for example]:

$$\frac{\nu}{h} \nabla^2 \zeta + \frac{1}{\rho_0 h} \mathbf{k} \cdot \nabla \times \left(\frac{\tau_w - \tau_b}{h} \right) = \frac{D}{Dt} \left(\frac{f + \zeta}{h} \right) \quad (5)$$

$$\approx \hat{v} f \frac{d}{dy} \left(\frac{1}{h} \right) + \hat{\mathbf{u}} \cdot \nabla \left(\frac{\zeta}{h} \right) \quad (6)$$

350 where $h = h(y)$ is the water column thickness, $\zeta = \partial \hat{v} / \partial x - \partial \hat{u} / \partial y$ is the relative
 351 vorticity, ν is the kinematic viscosity, ρ_0 is a reference density, τ_w is the surface stress,
 352 τ_b is the bottom stress, and \mathbf{k} is the unit vector pointing in the upwards vertical. We col-
 353 lectively refer to the terms on the left-hand side of (5) as viscous sources of BPV, and
 354 the first and second terms on the right-hand side of (6) as planetary and relative sources
 355 of BPV, respectively. In (5)–(6), $f = 2\Omega \sin \theta$ is the Coriolis frequency, where $\Omega = 7.2921 \times$
 356 10^{-5} is the rotation rate of the Earth and θ is the longitude. In practice, the relatively
 357 small size of the idealized domain means that θ , and thus f , can be assumed constant.
 358 The approximation (6) results from this assumption, alongside that of a zonally uniform
 359 water column thickness, and steady state conditions.

360 Equation (5) implies that in steady, inviscid flow with no bottom or surface stress,
 361 a water column advected by the flow will conserve its barotropic potential vorticity (BPV),
 362 $(f + \zeta)/h$. In our idealized domain, water column thickness is uniform in the zonal di-
 363 rection, i.e. h varies only in the meridional direction (figure 3c). As flow travels in the
 364 meridional direction, it crosses $1/h$ contours, so another source is required to balance the
 365 resulting BPV production. This can be achieved by adjusting relative vorticity, ζ , but
 366 in places where that balance cannot hold, viscous stresses intervene to complete the BPV
 367 balance. Plots of $1/h$ (figure 3c), $(f + \zeta)/h$ (figure 3d), and the barotropic stream func-
 368 tion (figure 3c, d) allow us to determine where in our domain each of the terms in equa-
 369 tion (5) play an important role. In regions where barotropic streamlines follow east-west
 370 aligned contours of constant water column thickness (figure 3c), relative and viscous sources
 371 of vorticity are small; where contours of constant BPV (colors in figure 3d) deviate from
 372 these east-west aligned f/h contours, relative vorticity plays an important role; finally,
 373 viscous stresses play an important role where barotropic streamlines (lines in figure 3d)
 374 deviate from contours of constant BPV (colors in figure 3d).

375 The ice front and the seabed ridge are the two predominant discontinuities in the
 376 water column thickness, and therefore act as BPV barriers: in order to cross these fea-
 377 tures in a meridional direction, barotropic flow must either change its relative vorticity
 378 or be subject to viscous stresses. These BPV barriers divide the domain up into three
 379 regions: inshore of the ridge, offshore of the ridge (but under the ice shelf, referred to
 380 as the ‘outer cavity’), and the open ocean.

381 In the open ocean, the combination of boundary restoring to salty water at the re-
 382 gion’s northern boundary and ice shelf freshwater influx at its southern boundary tilts
 383 the isopycnals, resulting in a cyclonic circulation. Note that, except for in the vicinity
 384 of the ice front, the gyre in the outer region has uniformly spaced streamlines (figure 3c):
 385 the flow is not faster along the lateral boundaries than it is on the north and south bound-
 386 aries. This corresponds to a uniform the relative vorticity, which is consistent with the
 387 approximately constant water column thickness in the interior of this region. At the ice
 388 front, there is a vertical wall. In any flow crossing this wall, relative vorticity cannot bal-
 389 ance the planetary BPV source (the flow cannot gain or lose vorticity over a zero length
 390 scale). Instead, the requirement for sudden shear causes viscous terms (left-hand side
 391 of (5)) to arise: the flow uses viscous sources to balance the planetary vorticity source
 392 as it crosses the ice front (seen as deviations between colors and contours in figure 3d).
 393 In the simulations, the gyre in the open ocean spins up until the shear at the ice front
 394 generates enough viscosity to permit barotropic flow to cross the ice front. This allows
 395 the heat flux, which causes melting thus tilting the isopycnals, to be maintained.

For the same reasons as in the open ocean (boundary restoring versus ice shelf fresh-water flux), the barotropic dynamics inshore of the ridge are also dominated by a large cyclonic gyre. It is interesting to note, however, that the circulation in this region is subtly different from the open ocean. This is ultimately because north-south flow in the inner cavity requires contours of constant water column thickness to be crossed: a source of BPV is required to balance the associated planetary vorticity source. To see this, consider the south-west quadrant of the inner cavity: when the flow is northward, into a thicker water column, the planetary source term is positive ($f < 0, \hat{v} > 0, d(1/h)/dy < 0$); one way in which a relative vorticity source can balance this with a negative value is if the flow gains cyclonic (negative) vorticity ($\hat{v} > 0, \partial\zeta/\partial y < 0$). This can be extended to the other quadrants: if the flow is heading southwards, then the sign of these terms switches, and if the flow is heading into a thinner water column, they switch again. In response, the relative vorticity becomes more negative in the south-west and north-east quadrants, and less negative in the north-west and south-east quadrants. These changes explain why the flow is intensified on the eastern and western boundaries: the flow must intensify (streamlines converge) to produce the required relative vorticity changes, i.e. the meridional topography variation is concomitant with zonal intensification of the meridional flow.

The outer cavity sits between the two regions hosting strongly topographically constrained circulations to its north and south. There is little flow in this region: the anti-cyclonic circulation that forms there (figure 3c) is much weaker than that in the open ocean or inshore of the ridge. This flow is not strong enough to generate the shear, and thus vorticity, that would be required at the ridge crest to balance planetary vorticity in southward flow across it (note the zero barotropic contour at the ridge crest, figure 3b). Just offshore of the ridge, flow is directed eastwards, parallel to the ridge crest. Where this jet meets the eastern domain boundary, the baroclinic component of flow provides the region inshore of the ridge with warm water from offshore of the ridge (figure 3b). However, the total flux across the ridge provided by this baroclinic flow (approximately 0.01 Sv) is small in comparison with the typical barotropic fluxes in the cavity, which are on the order of 0.3 Sv (figure 3c), i.e. the boundary current flushing of the inner cavity is relatively weak in comparison with the inner cavity circulation.

In the absence of significant flow across the ridge, the inshore side of the ridge hosts meltwater, which is recirculated rather than flushed out. Warm water entering the region inshore of the ridge at the eastern boundary mixes with this meltwater as it crosses the ridge, causing it to be lightly modified and resulting in a bottom temperature that is slightly cooler (approximately 0.8°C) inshore of the ridge than offshore (approximately 1.3°C, see figure 3b, e).

In summary, in the baseline simulation, which has a strong BPV barrier restricting CDW access to the inner cavity, strong cyclonic gyres are spun up in the open ocean and in the region inshore of the ridge, while in the outer cavity, the circulation is weak. The two cyclonic gyres are dynamically disconnected from one another, and barotropic flow is unable to cross the ridge. A baroclinic current at the eastern boundary of the ridge crest provides a modest source of lightly modified CDW, and thus heat for melting, to the region inshore of the ridge. The hosting of cold meltwater on the ice-ocean interface inshore of the ridge means that high melt rates are restricted to a region just downstream of the grounding line.

4 Melt Response to Calving

In this section, we describe how, and why, the inner cavity melt rate responds when the ice shelf is sequentially calved from the baseline configuration. The inner cavity melt rate as a function of the calved length l_c is shown in figure 4a. We see that, while the ice shelf front is located far offshore of the ridge ($l_c < 14$ km), removing sections of ice

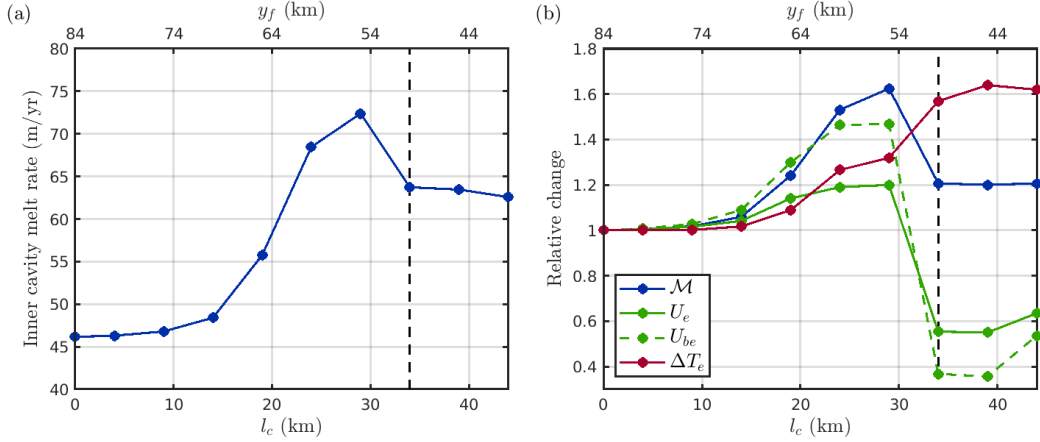


Figure 4. (a) Mean inner cavity melt rate as a function of the calved length l_c . The black dashed line indicates the position of the ice front when it is located directly above the seabed ridge. (b) Velocity-thermal driving decomposition: decomposition of changes in inner cavity melt rate relative to the baseline simulation into changes associated with boundary layer speed U_e [green curve, equation (7)] and thermal driving ΔT_e [red curve, equation (8)]. The blue curve indicates the change in melting relative to the uncalved simulation [equation (9)]. The green dashed line indicates the barotropic velocity effect U_{be} [equation (10)].

results in only a weak increase in the inner cavity melt rate. However, as the ice shelf front is retreated further towards the ridge, the melt rate increases more strongly with calving, reaching a maximum of 73 m year^{-1} (70% larger than in the baseline simulation) when the ice shelf is located approximately 5 km north of the ridge crest. Perhaps surprisingly, retreating the ice front slightly further to sit directly above the ridge crest results in a significant decrease in the inner cavity melt rate of approximately 15% (from 73 m year^{-1} to 64 m year^{-1}). Finally, the inner cavity melt rate is approximately independent of ice front position when the ice front is located inshore of the ridge ($l_c > 34 \text{ km}$).

To understand the reasons for this melt response to calving, it is instructive to return to equation (2), which indicates that the melt rate is proportional to the product of the boundary layer velocity and thermal driving. To investigate the relative roles of variations in both of these quantities in the changes to the inner cavity melt rate, we compute (Millgate et al., 2013)

$$U_e(l_c) = \frac{\int_{\text{IC}} u^*(x, y; l_c) \Delta T(x, y; l_c = 0) dx dy}{\int_{\text{IC}} u^*(x, y; l_c = 0) \Delta T(x, y; l_c = 0) dx dy}, \quad (7)$$

$$\Delta T_e(l_c) = \frac{\int_{\text{IC}} u^*(x, y; l_c = 0) \Delta T(x, y; l_c) dx dy}{\int_{\text{IC}} u^*(x, y; l_c = 0) \Delta T(x, y; l_c = 0) dx dy}, \quad (8)$$

where ‘IC’ refers to the inner cavity. Recall that $u^*(x, y; l_c)$ and $\Delta T(x, y; l_c)$ are the boundary layer velocity and thermal driving, respectively, that emerge from the experiment in which the ice front is located at $y = l_c$. The quantities in (7)–(8) are compared, for a given calved length l_c , to the relative change in melting over the baseline simulation,

$$\mathcal{M}(l_c) = \frac{\int_{\text{IC}} u^*(x, y; l_c) \Delta T(x, y; l_c) dx dy}{\int_{\text{IC}} u^*(x, y; l_c = 0) \Delta T(x, y; l_c = 0) dx dy}. \quad (9)$$

The quantities (7)–(9) are plotted in figure 4b as a function of l_c . Here, a melt response to calving that results exclusively from changes in thermal driving would be indicated by indistinguishable blue and red curves, and a green curve that takes the value

471 unity for all ℓ_c ; a melt response that results exclusively from changes in boundary layer
 472 velocity would be indicated by indistinguishable blue and green curves, and a red curve
 473 that takes the value unity for all ℓ_c . Henceforth, we refer to this comparison as a ‘velocity-
 474 thermal driving decomposition’.

475 The velocity-thermal driving decomposition (figure 4b) indicates that both changes
 476 in the boundary layer velocity and thermal driving play an important role in the melt
 477 response to calving, i.e. neither plays a dominant role. When the ice front is located off-
 478 shore of the ridge ($\ell_c < 30$ km), ice front retreat results in increases in both the bound-
 479 ary layer velocity and thermal driving: these increases are complementary, acting in uni-
 480 son to increase the inner cavity melt rate as calving proceeds. When the calving front
 481 is retreated to sit above the ridge, the thermal driving effect increases further, while the
 482 velocity effect decreases sharply, corresponding to a significant reduction in the bound-
 483 ary layer velocity at this point. This reduction in cavity circulation outweighs the increase
 484 in thermal driving, leading to an overall reduction in the inner cavity melt rate. When
 485 the ice shelf is calved further beyond the ridge, both the thermal driving and boundary
 486 layer velocity effects are approximately constant.

487 As mentioned, we shall assess the impact of calving on the behaviour primarily by
 488 considering its effect on the barotropic dynamics. To that end, we consider also the ‘barotropic
 489 velocity effect’, $U_{be}(\ell_c)$, which is computed as in (7) albeit with barotropic, rather than
 490 boundary layer, velocities:

$$491 U_{be}(\ell_c) = \frac{\int_{\text{IC}} |\hat{\mathbf{u}}(x, y; \ell_c)| \Delta T(x, y; \ell_c = 0) dx dy}{\int_{\text{IC}} |\hat{\mathbf{u}}(x, y; \ell_c = 0)| \Delta T(x, y; \ell_c = 0) dx dy}, \quad (10)$$

492 The agreement between $U_e(\ell_c)$ and $U_{be}(\ell_c)$ (figure 4b) suggests that changes in bound-
 493 ary layer velocity are closely related to changes in barotropic velocity, and provides sup-
 494 port for our use of barotropic framework when diagnosing the melt response to calving.

495 We diagnose the melt response to calving by considering two regimes. In the first
 496 regime, the ice front is located offshore of the ridge, $\ell_c < 30$ km and much of the be-
 497 havior is qualitatively similar to the uncalved case. The strong BPV barrier provided
 498 by the ridge and ice draft remains in place, and barotropic flow is unable to cross the
 499 ridge. The modest transport of warm water across the ridge, towards the inner cavity,
 500 occurs primarily via a baroclinic current at the eastern boundary, and the cavity circu-
 501 lation is vigorous. A topographically constrained cyclonic circulation is spun up inshore
 502 of the ridge, and this remains disconnected from the cyclonic circulation in the open ocean
 503 (figure 5a). There is little circulation in the outer cavity, which sits between these two
 504 cyclonic circulations.

505 As ice front retreat proceeds within this regime, the total meltwater flux reduces
 506 ($\ell_c = 0 - 29$ km in figure 5b–c). This reduction is the non-trivial outcome of a com-
 507 petition between a reduction in melting area and an increase in ocean temperature in-
 508 shore of the ridge as the ice shelf front is retreated. On the one hand, a smaller ice shelf
 509 means a reduction in the area over which melting is applied, promoting a reduced melt-
 510 water volume. On the other hand, a reduction in meltwater leads to reduced mixing be-
 511 tween the cold outflow and the warm inflow across the ridge, so the temperature of the
 512 warm water that enters the cavity increases, promoting an increased melt rate. We see
 513 that the effect of reductions in shelf area slightly outweighs the associated increase in
 514 melt rate when determining the overall meltwater flux. This is consistent with an increase
 515 in the thermal driving for $\ell_c < 30$ km (figure 4b). The associated increase in melt rate
 516 in the inner cavity leads to a stronger buoyancy flux, driving a slightly stronger circu-
 517 lation (increase in U_{be} in figure 4b), which itself enhances melting locally.

518 The second regime takes effect when the ice front is located above the seabed ridge
 519 crest. In this case, only a single PV barrier – the ice front, which sits at the ridge crest

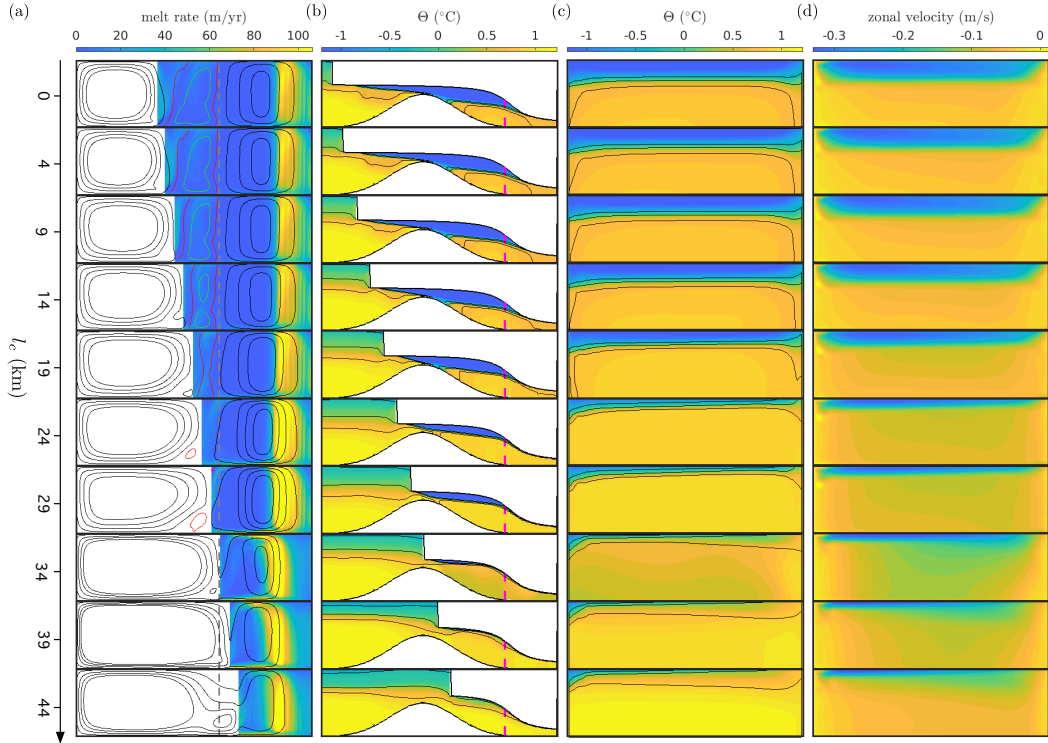


Figure 5. (a) Contour plots of melt rate (colors) and barotropic stream function (contours, black at -0.1, -0.3, -0.5, and -0.7 Sv levels, magenta at the 0 Sv level, and green at the 0.05 Sv level) in the idealized simulations with $P = 600$ m and $W = 100$ m. The calved length l_c increases from 0 km in the first row to 44 km in the final row. The white sections indicate open ocean. (b) Contour plots of potential temperature Θ (colors) and salinity (contours, at levels 34.2, 34.4, and 34.6 PSU, i.e. as in figure 3) taken along the centreline of the domain (magenta dashed line in figure 3a). The white section at the top and bottom of each subplot indicate the ice shelf and seabed ridge, respectively. (c) Contour plots of potential temperature (colors) and salinity (contours, at levels 34.2, 34.4, and 34.6 PSU) along a zonal section located 20 km downstream of the grounding line [magenta dashed line in (b)]. (d) As in (c) with colors indicating the zonal velocity. In each case, the color bar at the top of the column is appropriate for each row in the column.

– remains. The region offshore of the ridge, which previously hosted a weak circulation that separated the strong cyclonic gyres in the open ocean and in the region inshore of the ridge, no longer exists, permitting these two gyres to connect dynamically. The flow at the ridge crest now has a vigorous barotropic component. North-south barotropic flow across the ridge is therefore permitted because the planetary vorticity requirement associated with such flow can be satisfied by viscous sources associated with the ice front. Thus, a barotropic flow of approximately 0.1 Sv is able to cross the ridge at its eastern side (figure 5a), providing a large amount of heat to the inner cavity, while meltwater is efficiently flushed out of the cavity on the western side of the ridge. The region inshore of the ridge is almost entirely flooded with warm water (figure 5c). Although this means that there is much more heat available for melting (thermal driving effect increases when the ice front coincides with the ridge crest, figure 4b), the more efficient cavity flushing leads to a concomitant reduction in circulation (figure 5d). The latter outweighs the increase in thermal driving, ultimately leading to a reduction in the melt rate (figure 4b).

This picture remains when the ice front is retreated beyond the ridge. The gyres in the open ocean in the region inshore of the ridge are connected, permitting a significant barotropic flow to cross the ridge, which efficiently flushes the inner cavity with warm water. Thermal driving is enhanced, but cavity circulation is reduced, when compared to the situation in which the ice front is located offshore of the ridge. Melt rates become independent of ice front position once the ice front has retreated beyond the ridge. This indicates that the ridge only plays a role in the melt response to calving when it has an ice shelf overlying it (and the ridge-draft gap is small enough, as will be shown).

In summary, when the ice front is located offshore of the ridge, the ridge-draft BPV barrier prevents barotropic flow into the cavity and the inner cavity is weakly flushed with warm water via a baroclinic boundary flow at the eastern wall. As the ice front retreats, mixing with meltwater at this boundary is reduced; the heat content, and thus melt rate, in the inner cavity increases, leading to enhanced circulation and further increasing melt. As the ice front is retreated to the ridge crest, viscous vorticity exchanges at the ice front permit barotropic flow to cross the ridge. This flow efficiently flushes the inner cavity with warm water, providing a large amount of heat for melting, but is accompanied by a reduction in cavity circulation, which outweighs the increase in heat to ultimately reduce the inner cavity melt rate, compared to when the ice front is located offshore.

5 Effect of Cavity Geometry on Melt Response to Calving

In the previous section, we analyzed how the inner cavity melt rate responds to ice front retreat, and discussed the mechanisms responsible, in the case that the gap between the ice draft and ridge-crest is narrow. The strength of the topographic barrier that restricts warm water access to the inner cavity was identified as an important control on this response. In this section, we describe how this picture changes for larger values of W (in particular, for $W = 150$ m and $W = 200$ m), which lead to a weaker topographic barrier at the ridge crest.

Figure 6a shows the inner cavity melt rate as a function of calved length l_c for $W = 150$ m and $W = 200$ m in the $P = 600$ m case. We focus first on the $W = 200$ m case, which is characterized by inner cavity melt rates that are largely independent of the ice front position. As before, we use a barotropic framework to diagnose the behavior; barotropic contours are shown, alongside zonal and meridional cross-sections, for this case in figure 7 (the corresponding figure for $W = 100$ m is figure 5). Recall that, in the $W = 100$ m case, two regimes are observed, which are delineated by whether barotropic flow is able to cross the ridge or not: firstly, when the ice front is located offshore of the ridge, there is a ‘blocked’ regime: the strong BPV barrier that the ridge-crest and ice draft presents means that barotropic flow is prevented from crossing the ridge and, sec-

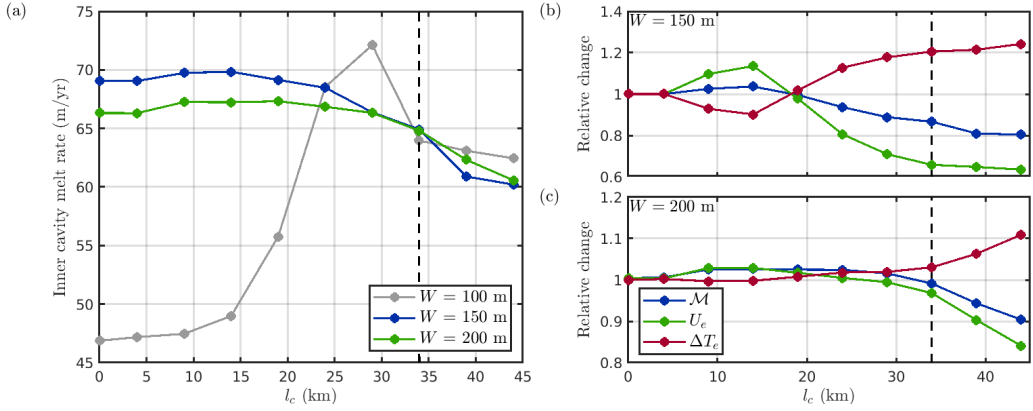


Figure 6. (a) Inner cavity melt rate as a function of the calved length l_c for $W = 100$ m (grey, as in figure 4a), $W = 150$ m (blue), and $W = 200$ m (green), each with $P = 600$ m. (b)–(c) Velocity-thermal driving decomposition for (b) $W = 150$ m and (c) $W = 200$ m. In each plot, the black dashed line indicates the position of the ice front when it is located directly above the seabed ridge.

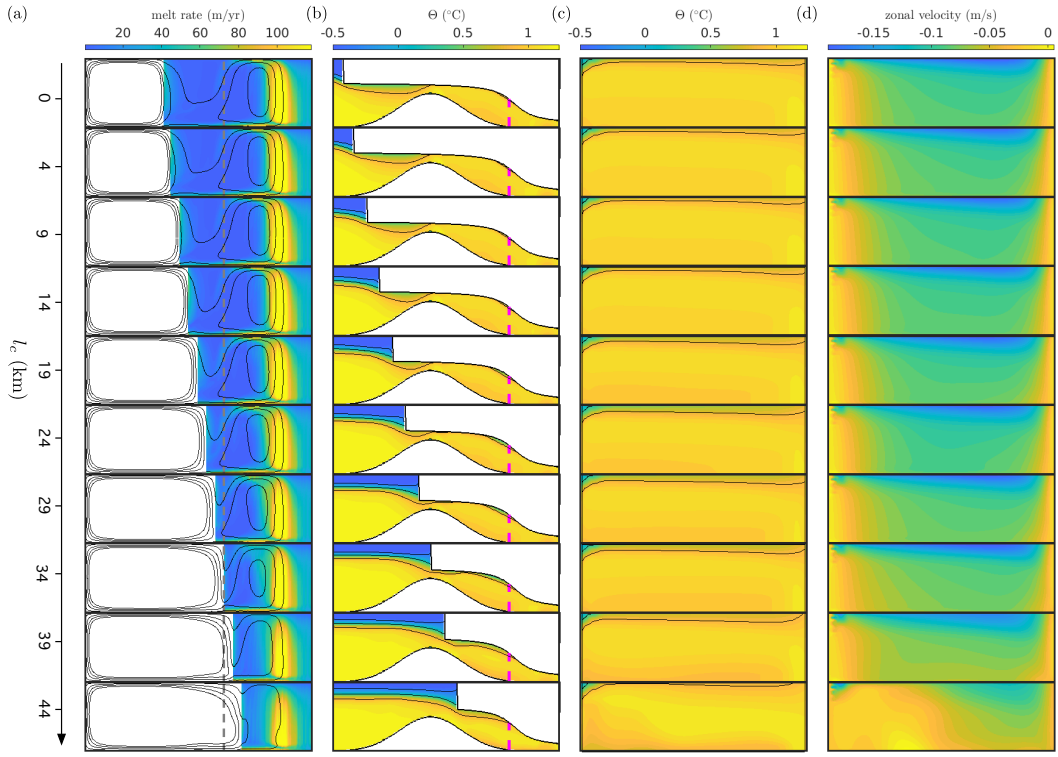


Figure 7. Response of ocean characteristics to calving in the idealized experiments with $P = 600$ m and $W = 200$ m. This plot is as in figure 5 for the experiment with $W = 200$ m.

571 ondly, there is a ‘connected’ regime: when the ice front is located above, or inshore, of
 572 the ridge, the gyres in the open ocean and inshore of the ridge become dynamically con-
 573 nected and barotropic flow is able to cross the ridge. In the $W = 200$ m case, however,
 574 the ridge-draft BPV barrier is much weaker than in the $W = 100$ m case, and barotropic
 575 flow is able to cross the ridge, even when the ice front is located offshore of the ridge (fig-
 576 ure 7a). The blocked regime is never realized: for all values of ℓ_c , the regions inshore and
 577 offshore of the ridge are dynamically connected. The system always behaves in a qual-
 578 itatively similar way to the $W = 100$ m connected regime, with the inner cavity effi-
 579 ciently flushed with modified CDW (figure 7b, c), and experiencing weak circulation. Ice
 580 front retreat therefore has little effect in the $W = 200$ m case. In particular, this re-
 581 moves the tendency for both increasing temperature and circulation that we see in the
 582 $W = 100$ m case as the ice front is retreated towards the ridge. This invariance to ice
 583 front position also holds for larger ridge-draft gaps ($W > 200$ m), a finding that is con-
 584 sistent with the results of De Rydt et al. (2014).

585 The $W = 150$ m case sits between the strong response to calving for $W = 100$ m,
 586 and the weak response to calving for $W = 200$ m. There are several similarities with
 587 the $W = 100$ m case: there is a reasonable sensitivity to ice front position (although
 588 it is somewhat smaller than in the $W = 100$ m case), the inner cavity melt rate reaches
 589 a maximum when the ice front is located offshore of the ridge crest, and the reduction
 590 in inner cavity melt rate for values of ℓ_c above that at which the maximum melt rate is
 591 attained results from a reduction in the inner cavity circulation that outweighs an in-
 592 crease in thermal driving (figure 6b). In contrast to the $W = 100$ m case, however, this
 593 scenario does not display a threshold-like behavior, where the inner cavity melt rate drops
 594 suddenly as the calving front reaches the top of the ridge. The weaker BPV barrier in
 595 the $W = 150$ m case means that, as in the $W = 200$ m case, the blocked regime is never
 596 realized; the threshold behavior, which occurs at the transition between the two regimes,
 597 is therefore suppressed.

598 6 Effect of Hydrographic Conditions on Melt Response to Calving

599 Before moving on to assess how the inner cavity melt rate responds to calving in
 600 the realistic simulations, we briefly consider how the picture presented in the previous
 601 two sections changes depending on the choice of hydrographic forcing. Since we consider
 602 a constant ridge height, variations in the difference between the pycnocline depth and
 603 the depth of the ridge crest, which we expect to be a key driver of the quantity of warm
 604 water that is able to spill over the ridge and into the inner cavity, is captured here by
 605 variability in the value of P (figure 2).

606 The inner cavity melt rate and velocity-thermal driving decomposition for the ex-
 607 periments with $P = 700$ m (hydrographic forcing as in the dashed profiles in figures 2b
 608 and c) and with $P = 800$ m (dot-dashed profiles) are shown in figure 8a and b, respec-
 609 tively. The results for $P = 700$ m are similar to those for $P = 600$ m: for the narrow-
 610 est gap ($W = 100$ m), the inner cavity melt rate is sensitive to the ice front position,
 611 increasing rapidly as the ice front is retreated towards the ridge crest, before dropping
 612 off sharply when the ice front reaches it, and does not change under further ice front re-
 613 treat beyond the ridge. In addition, the sensitivity of melt rate response to calving re-
 614 duces as the gap widens. A velocity-thermal driving decomposition for the experiments
 615 with $P = 700$ m (not shown) is qualitatively similar to the $P = 600$ m case discussed
 616 above, suggesting that the mechanisms for the response are as discussed in §4. The sim-
 617 ilarity between the $P = 600$ m and $P = 700$ m cases is perhaps unsurprising when
 618 framed in terms of the relationship between the depth of the pycnocline and the height
 619 of the ridge crest: in both cases, the CDW layer extends all the way to the top of the
 620 ridge (see figure 2) and thus the seabed ridge alone does not provide a significant bar-
 621 rier to CDW access to the inner cavity.

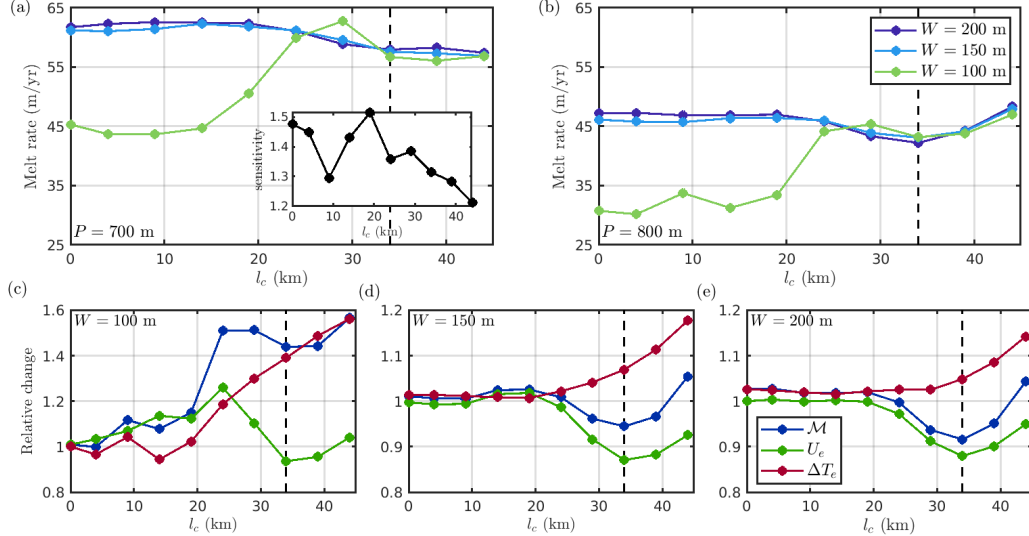


Figure 8. (a)–(b) Inner cavity melt rate as a function of calved length l_c in idealized simulations with (a) $P = 700$ m and (b) $P = 800$ m. Colors correspond to different values of W , as indicated by the legend in (b). The black dashed line indicates the location of the crest of the seabed ridge. The inset in (a) shows the sensitivity to the pycnocline position – the ratio of the inner cavity melt rate for $P = 700$ m and $P = 800$ m [i.e. the ratio of the data represented by the green lines in (a) and (b)] – as a function of the calved length l_c . (c)–(e) Velocity–thermal driving decompositions (as in figure 4) for the $P = 800$ m data shown in (b): (c), (d), and (e) correspond to the results for $W = 100$ m, $W = 150$ m, and $W = 200$ m, respectively, as indicated.

In the $P = 800$ m case, while the ice front is located offshore of the ridge, the melt rate is either constant, or increases, as the ice front is retreated, depending on the value of W (figure 8b). A reduction in the ice-ocean boundary layer velocity is responsible for a slight drop in inner cavity melt rates as the ice front is retreated towards the ridge crest (figure 8c–e), as in the $P = 700$ m and $P = 600$ m cases. Beyond this point, the $P = 800$ m case differs from the $P = 600$ m and $P = 700$ m cases: retreating the ice front beyond the ridge results in an increase in the inner cavity melt rate (figure 8b), which is associated with a reversal of the reduction in boundary layer velocity (figure 8c–e) (i.e. the boundary layer velocity increases on average when the ice front is retreated beyond the ridge). The important difference in this case is that the seabed ridge alone is able to provide a significant barrier that prevents warm water from reaching the inner cavity (the CDW layer in the outer cavity does not extend over the top of the ridge, see figure 9). As calving proceeds beyond the ridge, the thermal driving does not saturate (as in all the cases discussed above), but continues to increase, and the concomitant increase in glacial melt results in a stronger circulation (figure 8c).

7 Assessing the Melting Response of PIIS to Calving

The experiments described in §2–6 reveal how melt rates near the grounding line in idealized geometries with a uniform ridge-draft gap may respond sensitively to calving, depending on the thickness of the ridge-draft gap. These idealized experiments inform our understanding of similar experiments in a realistic domain, which are designed to assess the response of melt rates to PIIS calving. In this section, we describe these experiments, and present and analyze the results.

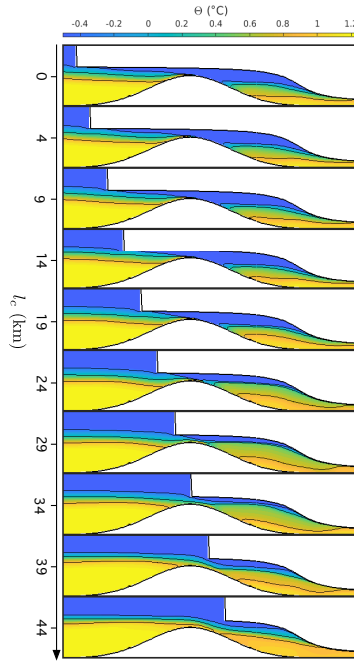


Figure 9. Meridional cross-sections, as in figure 5b for the simulation with $P = 800$ m, $W = 100$ m.

644

7.1 Experiment Details

Our experiments with a realistic setup are designed to assess the possible response of PIIS melt rates to calving in practice. To do so, we solve for the three-dimensional, quasi-steady ocean circulation and associated melt rates simultaneously in a PIG cavity geometry [from Dutrieux et al. (2014), and described briefly below], using the ocean model described in §2.1. We consider six different ice shelf topographies, each of which has a unique ice front position. The locations of these ice fronts are shown in figure 10: the first experiment ('2009' labelled curve in figure 10a) uses an ice shelf geometry that corresponds to PIIS in 2009 (Dutrieux et al., 2014). The second experiment ('2020' labelled curve in figure 10a) uses the 2009 ice shelf draft, but with a section of ice removed so that the ice front matches that obtained in 2020, whose position is determined from a Sentinel 2 mosaic of PIG. The four further experiments similarly use the 2009 ice shelf draft but with sections of fast flowing ice (i.e. within the shear margins) removed (figure 10). We stress that, as in the idealized experiments, the ice thickness, and thus grounding line position and ice shelf draft, at existing shelf locations remains the same in each experiment, and only the ice front position varies.

The sub-ice shelf cavity geometry we use is computed from the ice and seabed geometry, as described by Dutrieux et al. (2014). Briefly, the ice shelf geometry is calculated from a 40 m-resolution digital elevation model (DEM) of the ice freeboard from 2008 (Korona et al., 2009), which is adjusted with a constant median bias from observations obtained from the Autosub underwater autonomous vehicle (Jenkins et al., 2010). The DEM assumes freely floating ice throughout the shelf, which may reduce its accuracy close to the grounding line. Over the continental shelf, the seabed geometry is well known from ship echo-sounding (Dutrieux et al., 2014), while in the cavity it is calculated from an inversion of gravimetry data and corrected point-wise using the median difference between the depth from the gravimetry inversion and the Autosub observations.

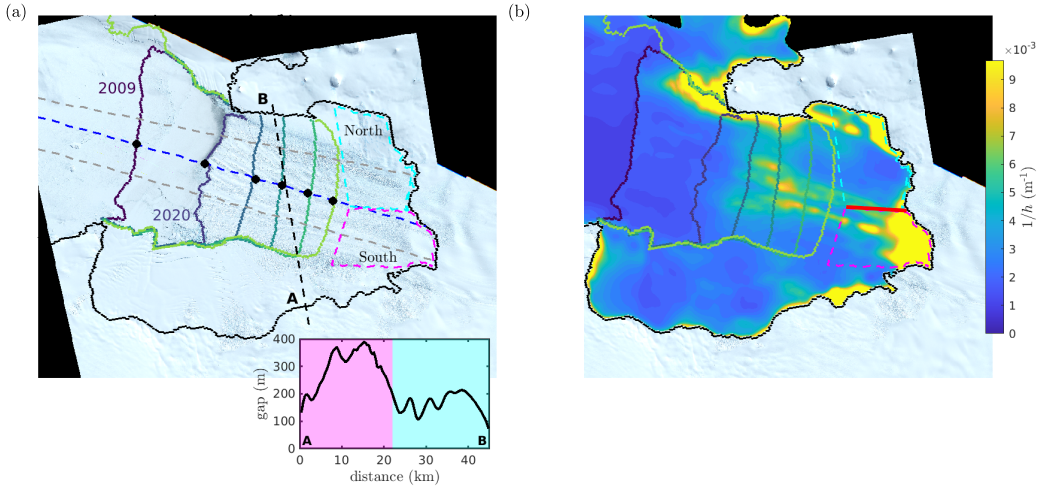


Figure 10. (a) Ice front positions used in experiments designed to assess the response of the PIIS melt rate to calving. Each experiment considers to a different ice front position, indicated by the curves in the purple to green colormap; labelled dark purple and dark blue ice fronts correspond to the 2009 and 2020 front positions, respectively. The solid black line indicates the location of the 2009 grounding line from Joughin et al. (2010). The blue dashed line roughly indicates the centreline of the cavity, along which the calved length – the difference between the ice front in the respective experiments and the 2009 ice front – is measured, and the black dashed line approximately indicates the peak of the seabed ridge. The cyan (north) and magenta (south) boxes indicate the inner cavity regions considered in the experiments (see main text). Inset: plot of the (vertical) gap between the ridge crest and the ice draft, measured along the black dashed line in the main figure. Cyan and magenta shaded sections correspond to locations north and south of the blue dashed centreline, respectively. The background image is a Sentinel 2 mosaic from November 2020. (b) Inverse water column thicknesses $1/h$ used in the experiment with the 2009 ice front. Ice front positions, inner cavity regions, and black dashed ridge crest are as in (a). Note that the boundary between the inner cavity regions (solid red line) is approximately aligned with a region of locally enhanced $1/h$, indicating the presence of a barotropic potential vorticity barrier between the north and south inner cavity regions.

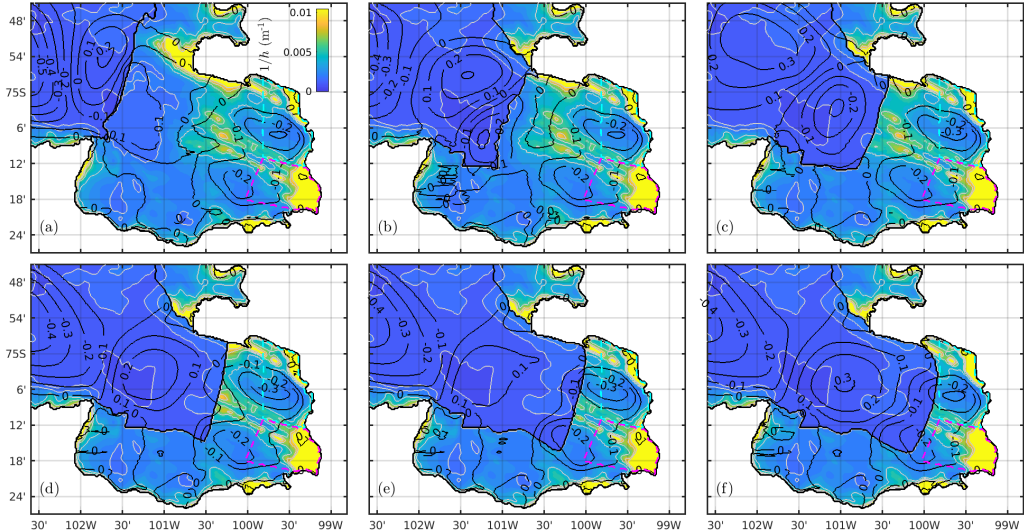


Figure 11. Simulated barotropic stream function (labelled black contours) and inverse water column thickness $1/h$ (colors and gray contours at levels corresponding to 200, 400, 600, 800, and 1000 m water column thickness). Magenta and cyan dashed boxes indicate the extent of the north and south inner cavity regions, respectively.

We consider a single hydrographic forcing, corresponding to observed 2009 conditions in Pine Island Bay (dark grey lines in figure 2b–c), to which the ocean is restored far from the ice shelf. All model parameters, and the spin-up procedure, are as in the idealized experiments, as described in §2.1. In particular, we take the drag coefficient in the three-equation formulation of melting to be 4.5×10^{-3} ; this value is tuned so that the total meltwater flux in the simulation with the 2009 geometry ($86 \text{ km}^3 \text{ year}^{-1}$) closely matches the estimated observed total meltwater flux for 2009 ($80 \text{ km}^3 \text{ year}^{-1}$) (Dutrieux et al., 2014).

As mentioned, the ridge-draft gap under PIIS is not uniform but varies from approximately 100 m at its narrowest to 400 m at its widest. The ridge-draft gap (inset in figure 10) can be approximately partitioned into a northern section, where the gap is relatively thin, and a southern section, where the gap is relatively thick. A region of locally elevated f/h running east-west (solid red line in figure 10b) meets the north-south aligned seabed ridge at the junction between these wide and narrow sections (see figure 10); this east-west aligned section is created by a thick ice keel in the center of the ice stream and extends all the way to the grounding line, partitioning the region inshore of the north-south aligned ridge into a northern inner cavity (cyan box in figure 10a) and a southern inner cavity (magenta box). The east-west aligned section of locally elevated f/h provides a PV barrier between the two inner cavity regions, which are therefore approximately dynamically disconnected (figure 11a). In the following, we therefore evaluate the melt response to calving in the two inner cavity regions separately.

7.2 Results

Cavity circulation (figure 11a) and melt rates (figure 12a) in the uncalved (2009) experiment are qualitatively similar to the corresponding baseline idealized experiment: melt rates are concentrated near to the grounding line, reaching a peak of approximately 120 m year^{-1} several kilometers downstream of it, while remaining below 20 m year^{-1} over

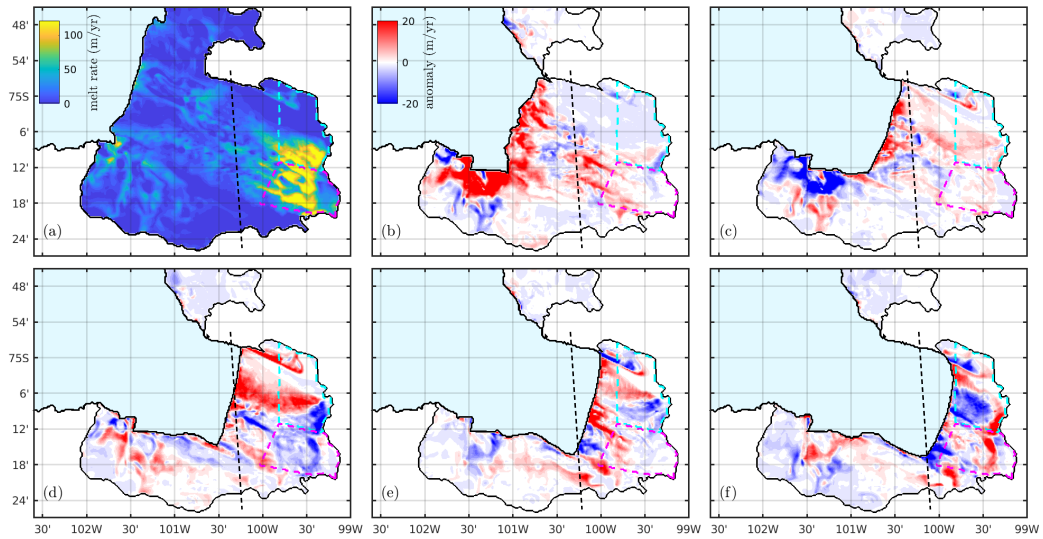


Figure 12. (a) Simulated melt rate in the 2009 Pine Island geometry. Cyan and magenta dashed boxes [also in (b)–(f)] indicate the north and south inner cavity regions (see figure 10), where the highest melt rates are concentrated. (b)–(f) Non-cumulative melt rate anomaly in the simulations (i.e. measured relative to the previous panel). The colorbar in (b) is appropriate for each of (b)–(f). Note that melt rate anomalies in (b) are saturated to a maximum of 20 m year^{-1} in the vicinity of the ice front (the maximum anomaly is approximately 30 m year^{-1}). In each case, the ice shelf front and 2009 grounding line, which are from Joughin et al. (2010)), are shown as a solid black line, and an estimate of the location of the ridge crest is shown as a black dashed line.

the majority of the shelf. This pattern of simulated melt rates under PIIS is consistent with observations (Dutrieux et al., 2013) and other numerical simulations of cavity circulation under PIIS (Heimbach & Losch, 2012, for example). Cyclonic circulation spins are spun up within both inner cavity sections, and in the open ocean offshore of the ice front, while a weak anti-cyclonic circulation spins up in the outer cavity between the seabed ridge and the ice front. Barotropic stream function contours largely follow the contours of constant water column thickness (figure 11).

Figure 12(b)–(f) show the non-cumulative melt rate anomalies for the other five experiments. To be explicit, non-cumulative here means that red (blue, respectively) locations on these maps indicate areas in which the melt rate increases (decreases) when the ice front is retreated from its position in the next largest ice shelf, i.e. changes in melt are shown relative to the previous experiment in the series, rather than relative to the uncalved (2009) simulation.

When the ice front is retreated from its 2009 position to its 2020 position, melt rates within 10 km of the ice front increase significantly (figure 12b). This is attributed to high velocities associated with overcoming the topographic barrier at the new ice shelf front, as well as the formation of a reasonably strong gyre in the newly exposed open ocean which is covered by the ice shelf in the 2009 configuration (figure 11b). This double gyre pattern is qualitatively similar to observations taken in PIB in 2020 (Yoon et al., 2022). The gyre adjacent to the ice shelf results in a strong circulation along the ice front, which also provides a freshwater source to further enhance the flow. Melt rates in both inner cavity regions do not change significantly when the ice front is retreated from its 2009 position to its 2020 position: the average melt rate in the northern and southern boxes increases by approximately 0.2 m year^{-1} and 1.2 m year^{-1} respectively (figure 13a, c).

Melt rates in the simulations with ice fronts retreated beyond the 2020 position display complex patterns of change, which include large regions of both positive and negative anomalies (figure 12c–f). Melt rates do not change significantly in the first ‘future’ scenario, in which the ice front is still located some way offshore of the ridge, in qualitative agreement with the idealized results. Melt rates in the vicinity of the northern shear margin increase dramatically when the ice front is retreated to a position that sits (approximately) above the seabed ridge (figure 12d), and this region of enhanced melt rates extends almost all the way to the grounding line. With the ice front immediately above the seabed ridge, the outer cavity region no longer exists; this is reminiscent of the idealized results in which there is a qualitative change in the behavior when the outer cavity disappears and the only remaining regions of closed f/h space are the inner cavity and the open ocean.

We show in figure 13a and c the mean melt rate as a function of calved length for the northern and southern inner cavity regions, respectively. In the northern inner cavity region, the mean melt rate remains approximately constant until the ice front approaches the seabed ridge, where they increase sharply, before remaining approximately constant as the ice front is retreated further. In the southern inner cavity region, the mean melt rate are less variable (in terms of percentage change), but the overall trend is that it increases while the ice front is located downstream of the seabed ridge, before dropping temporarily when the ice front is retreated to the ridge and subsequently increasing again. More quantitatively, the mean melt rate in the northern inner cavity region reaches a peak that is approximately 12% larger than present day, which is first realized when the ice front is retreated to the ridge (figure 13a). Although the mean melt rate in the southern inner cavity region decreases when the ice front is retreated to the ridge (figure 13c), the combined effect is to increase the melt rate in the entire inner cavity (inset in figure 13a). Indeed, the melt rate in the entire inner cavity increases approximately linearly after the first calving event (inset in figure 13a).

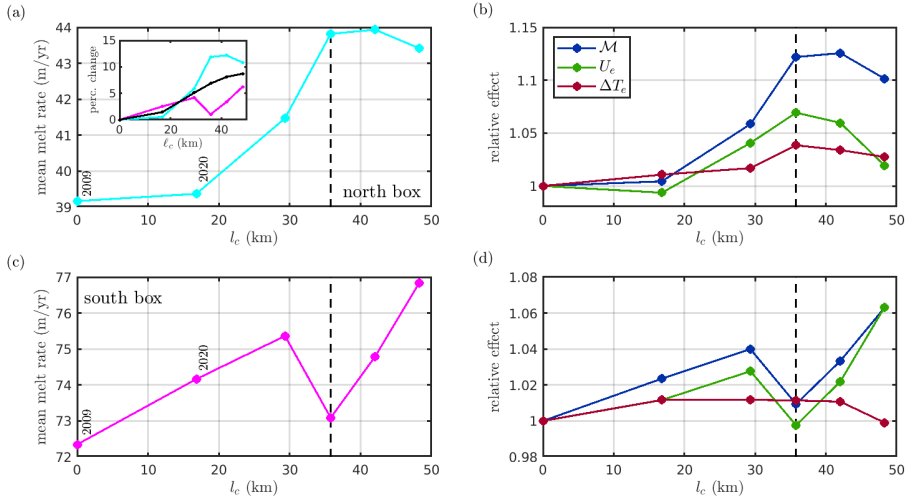


Figure 13. (a), (c) Average melt rate as a function of calved length l_c in experiments using a PIG geometry. Plots (a) and (c) correspond to the north and south regions of the inner cavity, respectively (cyan and magenta boxes in figure 10). The calved length l_c is the distance measured along the blue dashed line in figure 10a, taken relative to the 2009 ice front position (purple curve in figure 10a). The inset in (a) shows the percentage change in melt rate compared to the uncalved $l_c = 0$ km (2009) simulation as a function of calved length l_c for the north box (cyan curve), south box (magenta curve) and the entire inner cavity region (black curve). (b), (d) Velocity-thermal driving decomposition for the changes in melt rate shown in (a) and (c), respectively. As indicated by the legend in (b), blue, red, and green curves correspond to simulated changes \mathcal{M} , velocity effects U_e , and thermal driving effects ΔT_e , respectively. In each of the plots, the black dashed line approximately corresponds to the calved length when the ice front sits approximately above the ridge crest.

748 Our interpretation of these results is guided by the idealized simulations presented
 749 in §3–6. The northern inner cavity region is shielded by a relatively narrow gap between
 750 the seabed ridge and the ice draft (inset of figure 10a), and its melt response to calving
 751 behaves in a qualitatively similar way to idealized results with narrower gaps ($W \leq 150$ m).
 752 A velocity-thermal driving decomposition of these changes in melt rates (figure 13b) in-
 753 dicates that, as in the corresponding idealized case, both increases in thermal driving
 754 and velocity contribute to the increases in melt rate with calving while the ice front is
 755 located offshore of the ridge, and that a reduction in the boundary layer velocity is re-
 756 sponsible for the decrease in melt rates when the ice front is retreated beyond the ridge.
 757 This suggests that the enhancement in melt rates with calving while the ice front is lo-
 758 cated offshore of the ridge is driven by increased heat reaching the inner cavity and a
 759 concomitant increase in buoyancy forcing and thus circulation strength. As in the ide-
 760 alized case, when the calving front reaches the ridge, the trend of increasing melt rate
 761 with calving is reversed, although in this case that is observed as a saturation of the melt
 762 rates, rather than a strong reduction, as in the idealized case.

763 The southern inner cavity region sits inshore of a relatively wide gap between the
 764 seabed ridge and the ice draft (figure 10). As was the case for idealized simulations with
 765 wide gaps ($W \geq 200$ m), the mean melt rate is less sensitive to the ice front position
 766 than it is with a narrow gap, i.e. for the northern box (inset in figure 13a). This reduced
 767 response suggests that the southern inner cavity is dynamically connected to the outer
 768 cavities, regardless of ice front position; barotropic flow, providing significant heat to the
 769 inner cavity, is able to cross the ridge to the southern inner cavity in each simulation and
 770 thus calving only has limited influence.

771 8 Discussion

772 The results of the previous section suggest that the recent calving of PIG did not
 773 lead to increases in melting in either the shear margins or near the grounding line, which
 774 are particularly important for buttressing of the grounded ice sheet (Reese, Gudmunds-
 775 son, et al., 2018). Therefore, we do not expect that further buttressing losses associated
 776 with increased shelf melting will take place as a result of the recent calving. This lack
 777 of response might promote a negative feedback on ice shelf loss, encouraging its regrowth:
 778 the recent calving led to an acceleration of the grounded ice (Joughin et al., 2021), and
 779 thus an increase of the flux of ice into the shelf (assuming that ice thickness at the ground-
 780 ing line remained unchanged); to maintain a constant ice shelf mass balance, melting must
 781 therefore increase. The lack of increase in melting after the 2020 calving event might have,
 782 therefore, shifted the shelf mass balance towards positive, promoting regrowth of the ice
 783 shelf.

784 However, in all future scenarios considered here (all future ice front positions), fur-
 785 ther ice front retreat results in an increase in melting. This means that the first chain
 786 in the calving-melt feedback loop (calving leads to increased melting, reduced buttress-
 787 ing, acceleration and damage and thus further calving) is never broken, supporting the
 788 suggestion that such feedbacks are possible in West Antarctica. However, investigating
 789 the detailed response of the ice shelf mass balance to calving event requires the use of
 790 a coupled ice-ocean model, and is beyond the scope of this study.

791 Our results suggest that the mean melt rate in the inner cavity will increase ap-
 792 proximately linearly with calving beyond the 2020 front, and in particular, that the mean
 793 inner cavity melt rate will have increased by approximately 10% when the calving front
 794 sits above the ridge. A 10% increase in melt rates in the inner cavity region corresponds
 795 to a increased mass loss of approximately 3 Gt/year, and could represent an important
 796 contribution to ice shelf mass imbalance. In addition, this increased mass loss only re-
 797 flects changes the inner cavity regions, which are small fraction of the total ice shelf area;
 798 perhaps more important would be the effect of a 10% increase in melting in the vicin-

799 ity of the grounding line, which is particularly important for buttressing the ice sheet,
 800 as mentioned. In addition, the spatial pattern of changes in melting indicates that these
 801 increases are often focused around the shear margins, which, in addition to being par-
 802 ticularly important for buttressing, are the areas most prone to damage and where cracks
 803 in ice shelves are often initiated.

804 The magnitude of changes in melting in response to calving for the southern in-
 805 ner cavity region (for which the offshore ridge-seabed gap is wide) are similar to the cor-
 806 responding idealized simulations, i.e. reasonably small. For the northern inner cavity re-
 807 gion (narrow ridge-seabed gap), however, the magnitude of changes in melt with calv-
 808 ing is smaller than the corresponding idealized experiments predict, although the changes
 809 are qualitatively similar. We attribute this difference in magnitude to the complexities
 810 of the ice draft and seabed in the realistic simulations, and our splitting of the inner cav-
 811 ity into two subsections, which relies on the assumption that they are entirely dynami-
 812 cally disconnected. Although a strong BPV barrier exists between them, some flow is
 813 able to cross this barrier, providing a connection between the two regions. This inner
 814 cavity decomposition is a convenient tool that permits us to account for some of the ef-
 815 fect of the inhomogeneity in ridge-draft gap along its length, but further work is required
 816 to fully understand the role of variations in the ridge-draft gap in controlling basal melt
 817 rates on PIIS.

818 In addition, the sensitivity to cavity geometry identified in the idealized simula-
 819 tions means that the observed response may in fact be somewhat different to that pre-
 820 dicted here: if, for example, the ridge-draft gap is, in practice, smaller than that used
 821 in our realistic simulations (there are reasonable uncertainties in the ice draft and bathymetry
 822 beneath the shelf), the melt response to calving might be significantly larger. Further-
 823 more, the ice draft is not static but varies dynamically; advection of thicker sections of
 824 the ice shelf to the ridge crest would be expected to narrow the ridge-draft gap and thus
 825 increase the sensitivity of melt rates to calving, and vice versa for the advection of thin-
 826 ner sections of ice. Our idealized simulations also suggest that the melt-gap geometry
 827 feedback identified by (De Rydt et al., 2014), in which increases in the ridge-draft gap
 828 lead to an increase in melt rate and thus further ridge-draft gap widening, holds for any
 829 ice front position offshore of the ridge.

830 Variability in the depth of the pycnocline dominates ocean variability in the Amund-
 831 sen Sea on decadal timescales. Our idealized simulations point to a reduction in the sen-
 832 sitivity to pycnocline depth with calving once the ice front is reasonably close to the ridge
 833 provided that the gap is relatively thin ($l_c > 20$ km on the inset of figure 8a, which is
 834 appropriate for $W = 100$ m). However, for thicker gaps ($W > 150$ m), the sensitivity
 835 to pycnocline depth is largely independent of the ice front position (figure 8a, b). This
 836 conclusion is also borne out in our realistic experiments: supplementary experiments (not
 837 shown) using the realistic geometry, with the ocean restored to 2012 conditions in PIB
 838 far from the ice shelf, reveal that the ratio between the mean melt rate in the norther
 839 inner cavity region (narrow gap) for 2009 and 2012 boundary conditions is 1.52 for the
 840 largest ice shelf we consider, and 1.43 for the smallest. However, for the southern inner
 841 cavity region (wide gap), this ratio shows little change between the largest (1.29) and
 842 smallest (1.31) ice shelves we consider. The combination of a reduction in sensitivity in
 843 the northern box and an invariance in the southern box as calving proceeds suggests that
 844 PIIS melting may experience a reduction in the sensitivity to ocean conditions in the Amund-
 845 sen Sea in the future, assuming that the ice front continues to retreat. This motivates
 846 further study into future changes of the sensitivity of Amundsen Sea sector ice shelves
 847 to far field oceanic conditions.

848 The results presented in this paper have implications for melt rate parametriza-
 849 tions. At present, no melt rate parametrization is able to account for the position of the
 850 ice front, seabed topography, or indeed any BPV barrier, when computing the melt rate (Asay-
 851 Davis et al., 2017; Reese, Albrecht, et al., 2018; Bradley et al., 2022). Although the ex-

ample of PIG is somewhat extreme in this BPV barrier sense, we have demonstrated that the combination of seabed ridge and ice front position, which ultimately act as BPV barriers, can be an important control on the melt rate applied to an ice shelf. Ultimately, our results suggest that current melt rate parametrizations must be improved to account for the seabed ridge if they are to be trusted in future projections of PIIS.

It is important to note that MITgcm has a plethora of parameter choices and numerical settings, which might have an impact on the results of the simulations. These include choices of grid resolution, which are 400 m in the horizontal (to ensure mesoscale eddies are well resolved) and 10 m in the vertical. Simulations at higher vertical resolution (5 m) did not change the results significantly, although results were somewhat different for lower resolution (20 m); this is perhaps unsurprising given that exchange over the ridge crest, which we have shown to be important in controlling the inner cavity melt rate, is expected to be sensitive to vertical resolution. Agreement with the higher resolution simulations gives us confidence that the simulations presented here are appropriately resolving exchange processes over the ridge crest.

Finally, it is important to note that forcing in our simulations comes exclusively from buoyancy fluxes associated with ice shelf melting and restoring at the boundaries. In particular, the simulations include neither surface heat and freshwater fluxes nor sea ice, which would be expected to alter the horizontal density gradients and thus circulation in the open ocean. In addition, they do not include wind stresses, which provide a leading order control on heat content and circulation in Pine Island Bay (Dutrieux et al., 2014).

9 Summary

The central aim of this study is to understand how, and why, melt rates on Pine Island Ice Shelf might respond to calving events that have already taken place recently, and those that might occur in the future. To address this question, we have performed numerical simulations in both an idealized domain, and one that is representative of PIIS.

The idealized experiments allowed us to isolate parametric dependencies in the melt response to calving, and elucidate the mechanisms responsible for it. We identified a sensitive dependency on the cavity geometry via the parameter W that describes the gap between the seabed ridge and the ice draft: configurations with a narrow gap ($W \lesssim 150$ m) have a large response to calving, whereas those with wide gaps ($W > 150$ m) do not. We identified two key regimes for configurations whose cavities has a narrow gaps: in the first, the ice front is located offshore of the ridge, and the inner cavity melt rate increases with calving, and the change in melting for a given calved length increases as the ice front approaches the ridge. In the second regime, the ice front is located at or inshore of the ridge, and melt rates are significantly reduced compared to when the ice front is just offshore of the ridge if the pycnocline is relatively high, or enhanced further if the pycnocline is relatively deep. In contrast, for configurations with wide gaps, the melt rate is largely independent of the location of the ice front. Using a barotropic framework, we identified the roles of changes in circulation and thermal driving in the melt response to calving, and described how these roles are modulated by barotropic flow across the ridge, meltwater mixing, and barotropic potential vorticity barriers in the domain. Although these idealized results are intended to inform our understanding of melt rate changes beneath Pine Island Glacier, they can also be considered to be an archetype for situations in which the seabed geometry restricts the access of warm water to the grounding line of an ice sheet. This situation might be realized, for example, in ice sheet retreat over an over-deepened bed. In addition, the results for wide gaps suggest that melt rates are insensitive to ice front position in ice shelf cavities with no seabed ridge.

901 The idealized experiments informed experiments performed using a cavity geom-
 902 etry that closely resembles PIIS, designed to assess how melt rates on PIIS might respond
 903 to calving in practice. This geometry has two inner cavity regions, which are approxi-
 904 mately dynamically disconnected due to a thick ice keel across the center of the glacier.
 905 One of the inner cavity sections sits inshore of a narrow section of the ridge-draft gap;
 906 in this region the melt rate increases with calving while the ice front is located offshore
 907 of the ridge, before saturating with further calving beyond the ridge. In contrast, the
 908 other cavity section sits inshore of a wide section of the ridge-draft gap; there, the melt
 909 rate is largely independent of calving. Both of these observations are qualitatively con-
 910 sistent with the idealized simulations.

911 Our results demonstrate that the impact of calving on melt rates may represent
 912 an important, but as yet unexplored, contribution to the ice-ocean sensitivity of the West
 913 Antarctic Ice Sheet. They provide evidence that melt rates have not changed in response
 914 to recent calving events, but will increase linearly with future calving events. This in-
 915 creased mass loss, which is expected to take place in dynamically important regions of
 916 the ice shelf, might lead to a significant ice shelf mass imbalance. In addition, the con-
 917 stant increase in melt rate with retreat supports the possibility of a feedback loop in which
 918 calving leads to increased melting, reduced buttressing, acceleration and damage and thus
 919 further calving.

920 Acknowledgments

921 A. T. B. and D. T. B. are supported by the NERC Grant NE/S010475/1. J. D. R. is sup-
 922 ported by the TiPACCs project, which receives funding from the European Union's Hori-
 923 zon 2020 research and innovation programme under grant agreement no. 820575. NSF
 924 (through grant OPP-1643285) and the NASA MAP program provided support to P.D..

925 The simulations were performed using MITgcm at checkpoint c67u, which is pub-
 926 licly accessible at http://mitgcm.org/public/source_code.html. Files and code used
 927 to drive MITgcm and produce the figures in this paper are available at <https://github.com/alextbradley/PIG-melt-response-to-calving>.

929 The numerical simulations were carried out on ARCHER2, the U.K. national HPC
 930 facility (<http://archer2.ac.uk/>).

931 References

- 932 Arthern, R. J., & Williams, C. R. (2017). The sensitivity of west antarctica to the
 933 submarine melting feedback. *Geophys. Res. Lett.*, 44(5), 2352–2359.
- 934 Asay-Davis, X. S., Jourdain, N. C., & Nakayama, Y. (2017). Developments in sim-
 935 ulating and parameterizing interactions between the southern ocean and the
 936 antarctic ice sheet. *Curr. Clim. Ch. Rep.*, 3(4), 316–329.
- 937 Bradley, A. T., Williams, C. R., Jenkins, A., & Arthern, R. (2022). Asymptotic
 938 analysis of subglacial plumes in stratified environments. *Proc. Roy. Soc. A*,
 939 478(2259), 20210846. doi: 10.1098/rspa.2021.0846
- 940 Dansereau, V., Heimbach, P., & Losch, M. (2014). Simulation of subice shelf melt
 941 rates in a general circulation model: Velocity-dependent transfer and the role
 942 of friction. *Journal of Geophysical Research: Oceans*, 119(3), 1765–1790.
- 943 De Rydt, J., & Gudmundsson, G. H. (2016). Coupled ice shelf-ocean modeling and
 944 complex grounding line retreat from a seabed ridge. *J. Geophys. Res. Earth*
 945 Surf., 121(5), 865-880.
- 946 De Rydt, J., Holland, P. R., Dutrieux, P., & Jenkins, A. (2014). Geometric and
 947 oceanographic controls on melting beneath pine island glacier. *J. Geophys.*
 948 *Res. Oceans*, 119(4), 2420–2438.
- 949 De Rydt, J., Reese, R., Paolo, F. S., & Gudmundsson, G. H. (2021). Drivers of pine

- island glacier speed-up between 1996 and 2016. *Cryosphere*, 15(1), 113–132.
- Dutrieux, P., De Rydt, J., Jenkins, A., Holland, P. R., Ha, H. K., Lee, S. H., ... Schröder, M. (2014). Strong sensitivity of pine island ice-shelf melting to climatic variability. *Science*, 343(6167), 174–178.
- Dutrieux, P., Vaughan, D. G., Corr, H. F. J., Jenkins, A., Holland, P. R., Joughin, I., & Fleming, A. H. (2013). Pine island glacier ice shelf melt distributed at kilometre scales. *Cryosphere*, 7(5), 1543–1555.
- Gagliardini, O., Durand, G., Zwinger, T., Hindmarsh, R. C. A., & Le Meur, E. (2010). Coupling of ice-shelf melting and buttressing is a key process in ice-sheets dynamics. *Geophys. Res. Lett.*, 37(14).
- Gardner, A. S., Moholdt, G., Scambos, T., Fahnestock, M., Ligtenberg, S., van den Broeke, M., & Nilsson, J. (2018). Increased west antarctic and unchanged east antarctic ice discharge over the last 7 years. *Cryosphere*, 12(2), 521–547.
- Goldberg, D. N., Gourmelen, N., Kimura, S., Millan, R., & Snow, K. (2019). How accurately should we model ice shelf melt rates? *Geophys. Res. Lett.*, 46(1), 189–199.
- Grosfeld, K., Gerdes, R., & Determann, J. (1997). Thermohaline circulation and interaction between ice shelf cavities and the adjacent open ocean. *J. Geophys. Res. Oceans*, 102(C7), 15595–15610.
- Gudmundsson, G. H. (2013). Ice-shelf buttressing and the stability of marine ice sheets. *The Cryosphere*, 7(2), 647–655.
- Gudmundsson, G. H., Paolo, F. S., Adusumilli, S., & Fricker, H. A. (2019). Instantaneous antarctic ice sheet mass loss driven by thinning ice shelves. *Geophys. Res. Lett.*, 46(23), 13903–13909.
- Heimbach, P., & Losch, M. (2012). Adjoint sensitivities of sub-ice-shelf melt rates to ocean circulation under the pine island ice shelf, west antarctica. *Ann. Glaciol.*, 53(60), 59–69.
- Heywood, K. J., Biddle, L. C., Boehme, L., Dutrieux, P., Fedak, M., Jenkins, A., ... M. W. B. G. (2016). Between the devil and the deep blue sea: The role of the amundsen sea continental shelf in exchanges between ocean and ice shelves. *Oceanography*, 29(4), 118–129.
- Holland, D. M., & Jenkins, A. (1999). Modeling thermodynamic ice–ocean interactions at the base of an ice shelf. *J. Phys. Oceanogr.*, 29(8), 1787–1800.
- Jacobs, S. S., Hellmer, H. H., & Jenkins, A. (1996). Antarctic ice sheet melting in the southeast pacific. *Geophys. Res. Lett.*, 23(9), 957–960.
- Jacobs, S. S., Jenkins, A., Giulivi, C. F., & Dutrieux, P. (2011). Stronger ocean circulation and increased melting under pine island glacier ice shelf. *Nat. Geosci.*, 4(8), 519–523.
- Jacobs, S. S., Jenkins, A., Hellmer, H., Giulivi, C., Nitsche, F., Huber, B., & Guerroero, R. (2015). The amundsen sea and the antarctic ice sheet. *Oceanography*, 25(3), 154–163.
- Jenkins, A., Dutrieux, P., Jacobs, S. S., McPhail, S. D., Perrett, J. R., Webb, A. T., & White, D. (2010). Observations beneath pine island glacier in west antarctica and implications for its retreat. *Nat. Geosci.*, 3(7), 468–472.
- Jenkins, A., Shoosmith, D., Dutrieux, P., Jacobs, S., Kim, T. W., Lee, S. H., ... Stammerjohn, S. (2018). West antarctic ice sheet retreat in the amundsen sea driven by decadal oceanic variability. *Nat. Geosci.*, 11(10), 733–738.
- Joughin, I., Shapero, D., Smith, B., Dutrieux, P., & Barham, M. (2021). Ice-shelf retreat drives recent pine island glacier speedup. *Sci. Adv.*, 7(24), eabg3080.
- Joughin, I., Smith, B. E., & Holland, D. M. (2010). Sensitivity of 21st century sea level to ocean-induced thinning of pine island glacier, antarctica. *Geophys. Res. Lett.*, 37(20).
- Korona, J., Berthier, E., Bernard, M., Rémy, F., & Thouvenot, E. (2009). Spirit. spot 5 stereoscopic survey of polar ice: reference images and topographies during the fourth international polar year (2007–2009). *ISPRS J. Photogramm.*

- Remote Sens., 64(2), 204–212.

Lhermitte, S., Sun, S., Shuman, C., Wouters, B., Pattyn, F., Wuite, J., ... Nagler, T. (2020). Damage accelerates ice shelf instability and mass loss in amundsen sea embayment. *Proc. Nat. Acad. Sci.*, 117(40), 24735–24741.

Losch, M. (2008). Modeling ice shelf cavities in z coordinate ocean general circulation model. *J. Geophys. Res. Oceans*, 113(C8).

Marshall, J., Hill, C., Perelman, L., & Adcroft, A. (1997). Hydrostatic, quasi-hydrostatic, and nonhydrostatic ocean modeling. *Journal Geophys. Res. Oceans*, 102(C3), 5733–5752.

McDougall, T. J., Jackett, D. R., Wright, D. G., & Feistel, R. (2003). Accurate and computationally efficient algorithms for potential temperature and density of seawater. *J. Atmos. Ocean. Technol.*, 20(5), 730–741.

Millgate, T., Holland, P. R., Jenkins, A., & Johnson, H. L. (2013). The effect of basal channels on oceanic ice-shelf melting. *J. Geophys. Res. Oceans*, 118(12), 6951–6964.

Mouginot, J., Rignot, E., & Scheuchl, B. (2014). Sustained increase in ice discharge from the amundsen sea embayment, west antarctica, from 1973 to 2013. *Geophys. Res. Lett.*, 41(5), 1576–1584.

Pacanowski, R., & Philander, S. (1981). Parameterization of vertical mixing in numerical models of tropical oceans. *Journal of Physical Oceanography*, 11(11), 1443–1451.

Patmore, R. D., Holland, P. R., Munday, D. R., Naveira Garabato, A. C., Stevens, D. P., & Meredith, M. P. (2019). Topographic control of southern ocean gyres and the antarctic circumpolar current: a barotropic perspective. *Journal of Physical Oceanography*, 49(12), 3221–3244.

Pritchard, H. D., Ligtenberg, S. R. M., Fricker, H. A., Vaughan, D. G., van den Broeke, M. R., & Padman, L. (2012). Antarctic ice-sheet loss driven by basal melting of ice shelves. *Nature*, 484(7395), 502–505.

Reese, R., Albrecht, T., Mengel, M., Asay-Davis, X., & Winkelmann, R. (2018). Antarctic sub-shelf melt rates via pico. *The Cryosphere*, 12(6), 1969–1985.

Reese, R., Gudmundsson, G. H., Levermann, A., & Winkelmann, R. (2018). The far reach of ice-shelf thinning in antarctica. *Nat. Clim. Chang.*, 8(1), 53–57.

Rignot, E. (2008). Changes in west antarctic ice stream dynamics observed with alos palsar data. *Geophys. Res. Lett.*, 35(12).

Rignot, E., Jacobs, S., Mouginot, J., & Scheuchl, B. (2013). Ice-shelf melting around antarctica. *Science*, 341(6143), 266–270.

Rignot, E., Mouginot, J., Morlighem, M., Seroussi, H., & Scheuchl, B. (2014). Widespread, rapid grounding line retreat of pine island, thwaites, smith, and kohler glaciers, west antarctica, from 1992 to 2011. *Geophys. Res. Lett.*, 41(10), 3502–3509.

Rignot, E., Mouginot, J., & Scheuchl, B. (2011). Ice flow of the antarctic ice sheet. *Science*, 333(6048), 1427–1430.

Rignot, E., Mouginot, J., Scheuchl, B., Van Den Broeke, M., Van Wessem, M. J., & Morlighem, M. (2019). Four decades of antarctic ice sheet mass balance from 1979–2017. *Proc. Nat. Acad. Sci.*, 116(4), 1095–1103.

Rignot, E., Vaughan, D. G., Schmeltz, M., Dupont, T., & MacAyeal, D. (2002). Acceleration of pine island and thwaites glaciers, west antarctica. *Ann. Glac.*, 34, 189–194.

Seroussi, H., Morlighem, M., Larour, E., Rignot, E., & Khazendar, A. (2014). Hydrostatic grounding line parameterization in ice sheet models. *The Cryosphere*, 8(6), 2075–2087.

Shepherd, A., Wingham, D., & Rignot, E. (2004). Warm ocean is eroding west antarctic ice sheet. *Geophys. Res. Lett.*, 31(23).

Smith, J. A., Andersen, T. J., Shortt, M., Gaffney, A. M., Truffer, M., Stanton, T. P., ... Vaughan, D. G. (2017). Sub-ice-shelf sediments record history of

- 1060 twentieth-century retreat of pine island glacier. *Nature*, 541(7635), 77–80.
- 1061 Webber, B. G., Heywood, K. J., Stevens, D. P., Dutrieux, P., Abrahamsen, E. P.,
1062 Jenkins, A., ... Kim, T. W. (2017). Mechanisms driving variability in the
1063 ocean forcing of pine island glacier. *Nat. Commun.*, 8(1), 1–8.
- 1064 Yoon, S.-T., Lee, W. S., Nam, S., Lee, C.-K., Yun, S., Heywood, K., ... Bradley,
1065 A. T. (2022). *Meltwater feedback reduces ocean heat input to an antarctic ice*
1066 *shelf* (Vol. 13) (No. 306).